博士論文（要約）

Development of a markerless tumor prediction system using principal component analysis and multi-channel singular spectral analysis with real-time respiratory phase recognition in radiation therapy

（放射線治療におけるリアルタイム呼吸位相認識と主成分分析多チャンネル特異スペクトル解析によるマーカーレス腫瘍動体予測システムの開発）

チャタクリ　リトゥ　ブーサル

Chhatkuli Ritu Bhusal

Abstract

Image guided radiation therapy has improved the accuracy of tumor localization. Nevertheless, accuracy of the delivered dose to the moving target was often limited. Beam tracking was proposed to solve this issue; however, proposed techniques were based on infrared or implanted fiducial markers. It has been reported that the correlation between the marker and the tumor positions were not sufficiently high.

The purpose of this study was to develop a system to predict the tumor position in real-time based on images without using any markers.

As a preliminary study for this research, an algorithm for predicting the tumor position was developed using principal component analysis (PCA) and multi-channel singular spectral analysis (MSSA). Lung motion model based on PCA has been previously reported, which efficiently represents the lung motion in few principal components. However, they were used for the reconstruction. So far, prediction of images has not been considered. Hence in this study, the algorithm for image prediction was considered. For the algorithm development, first a set of four dimensional CT (4DCT) images acquired from a lung cancer patient were used. Since 4DCT images are not handled in real time, kilovolt (kV) fluoroscopic images were acquired from a moving phantom. In both case, the prediction result from PCA, MSSA shows a successful prediction in considerable time and with minimum error. The accuracy of the image prediction algorithm was verified using the cross correlation coefficient and structure similarity index.

Since the PCA and MSSA based tumor tracking was developed keeping in mind the gantry with fixed x-ray source and detector, a much more practical approach was considered next for the case of rotating gantry. This second approach was created keeping in mind the requirements in the clinics and hospitals. It is based upon template matching between the re-projected images from priorly acquired four dimensional cone beam CT (4D-CBCT) and real-time in-treatment projection images. Prior 4DCBCT acquisition is a part of treatment procedure for patient positioning in clinical sites recently

and in-treatment projection images are acquired for the verification purposes. The purpose of developing this phase recognition algorithm is to recognize the phase of tumor in real-time. This was performed with one dimensional phantom, 4D dynamic phantom and patient data. The case with flattening filter free beams were also analyzed. Removing flattening filters removes the beam-on time hence reducing the possibility of the normal tissue irradiation. The results indicate the successful phase recognition with significant accuracy. The verification for its accuracy was performed using cross correlation coefficient.

The image prediction system and 4D-CBCT based phase recognition was considered for static and rotating gantry respectively. Successful implementation of these systems is believed to provide a better precision in image guided radiation therapy.

Acknowledgement

Foremost, I would like to express my sincere thanks to my supervisor Professor Mitsuru Uesaka, Department of Bioengineering and Nuclear Professional School for his valuable guidance and supervision in the successful completion of this research. I sincerely appreciate his support, patience and motivation and understanding.

I would also express my gratitude to Associate Professor Kazuyuki Demachi, Department of Nuclear Professional School for his advice, guidance, and encouragement for this research.

I deeply thank my other advisor Dr. Akihiro Haga, head of medical physicists, Department of Radiology, the University of Tokyo hospital for his valuable guidance and leading me with his practical advice and in particular enlightening me the first glance of the research.

I express my sincere appreciation to Dr. Keiichi Nakagawa, also the member in my thesis committee and his team (Dr. Kanabu Nawa, Dr. Dousatsu Sakata, Dr. Taichi Magome and Mr. Masahiro Nakano) at University of Tokyo hospital for their advice and the support in the completion of this research.

Besides my advisors, I would like to thank the other members of my thesis committee; Prof. Hiroyuki Takahashi, Assoc. Prof. Yoshikazu Nakajima and Assoc. Prof. Masaki Sekino for their encouragement and the insightful comments.

My gratitude and sincere thanks to Dr. Kiyoshi Yoda, Elekta K.K. and Dr. Masatoshi Hashimoto, Ganken Ariake Hospital for their valuable guidance during the course of this research.

I would also like to convey my thanks to Prof. Kazuyoshi Koyama, Dr. Shinichi Yamashita and our lab secretaries Ms. Moe Sekiguchi, Ms. Kayako Shigematsu for their help throughout. My sincere thanks to all my lab members in Tokyo and Tokai for their support. My special thanks to the help and support from my lab mate late Mr. Kazuhiro Tagi who unfortunately is no more with us.

I would also like to acknowledge with gratitude Dr. Naoki Miyamoto, Assistant Professor, Hokkaido University Hospital, Dr. Koichiro Sugahara, Accuthera and Dr. Kazue Mizuno for their encouragement and support.

My sincere thanks to all the faculty and staff members at the Department of Bioengineering, the University of Tokyo, for their continuous support. It was a real pleasure to work with such lovely people.

I would like to thank the Graduate School of Engineering, the University of Tokyo, for provding me the SEUT fellowship, as a financial support to the successful completion of this research.

At last but not the least, I express my sincere appreciation to my family for their unconditional support, my parents for always being there for me, my parents-in-law for believing in me, my husband, Dr. Subas Chhatkuli for his support, patience and tolerance and my seven years old son Baibhav Chhatkuli for his patience and understanding.

Finally thanks to all those people who directly or indirectly have contributed to this research.

CONTENTS

LIST OF TABLES

LIST OF FIGURES

Chapter 1

Introduction

Cancer

Cancer (also known as malignant neoplasm or malignant tumor) is an uncontrolled or abnormal growth and spread of cells.

As of any other developing country cancer is increasing yearly in Japan. As of the year 2013, it is the leading cause of death in Japan (Fig. 1.1) [http://ganjoho.jp/data/]. Since the end of world war II, the mortality rate of infectious disease such as tuberculosis and pneumonia has decreased however the rate of life-style diseases such as cancer has increased [http://ganjoho.jp/data/]. It has been leading cause of death since 1981 accounting to 30 percent of all deaths recently.

In 2013, the cancer mortality rate (annual number of deaths per 100,000 population) was approximately 355 for males and 229 for females. According to the statistics compiled by the Ministry of Health, Labor and Welfare cancer accounts for one in every three deaths in Japan. Heart diseases, the second cause of death accounts for only about half the number of cancer deaths. Lung cancer became the major cause of cancer deaths among Japanese for the first time in 1998, surpassing stomach cancer, according to statistics compiled by the Ministry of Health, Labor and Welfare. The cancer site with the highest mortality rate were lung, stomach, colon/rectum, liver and pancreas for males and colon/rectum, lung, stomach, pancreas and breast for the females as shown in Fig. 1.2 [http://ganjoho.jp/data/].

Lung cancer is the highest among the males and second highest among the females after the colon and rectum are combined.

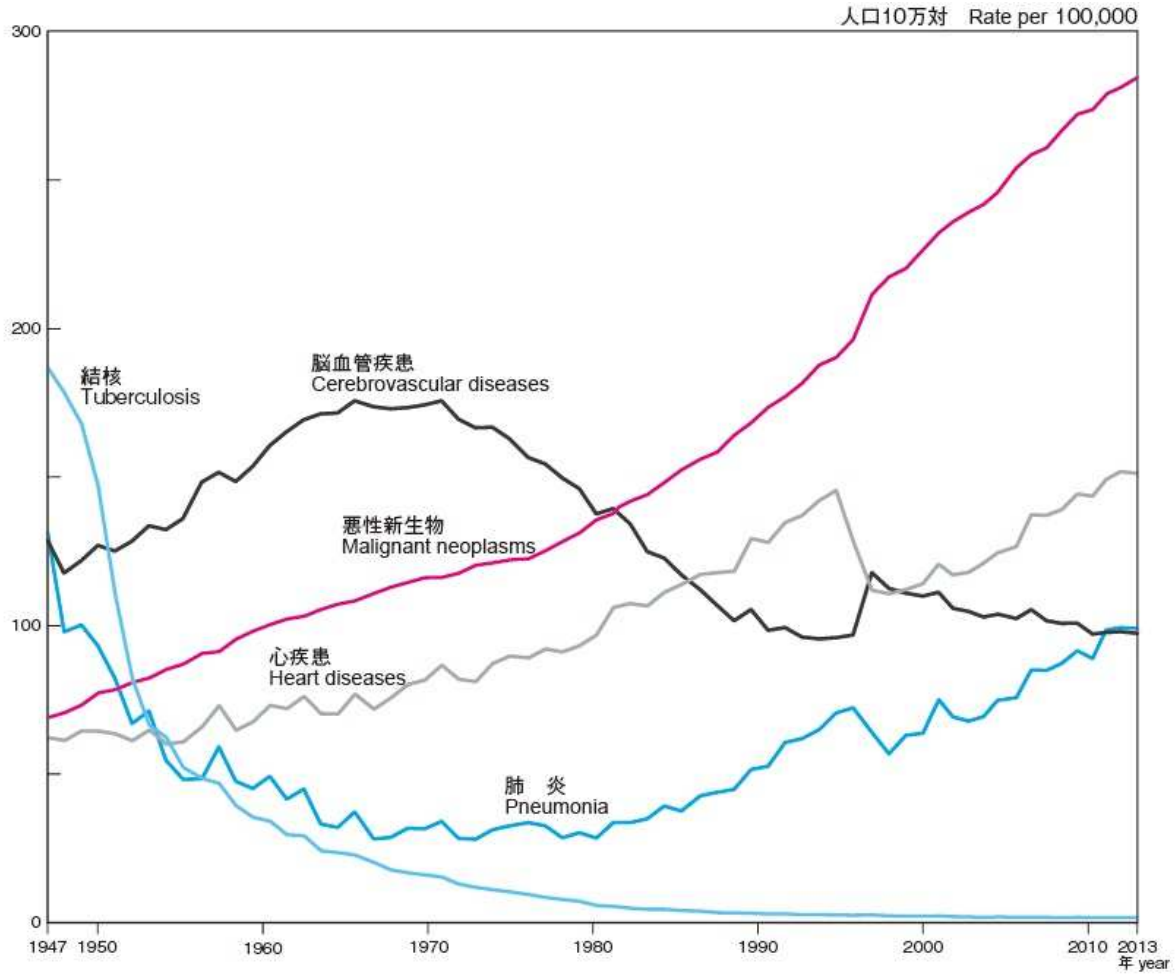

Figure 1.1: Cancer increasing yearly in Japan[Ganjoho (2014)].

1.1 Treatment Modalities

Treatment for cancer basically depends upon the cancers specific cell types, the area of the cancer and the patients medical conditions. There are basically three types of modalities in the treatment of cancer, surgery, and chemotherapy and radiation therapy. However, as shown in the schematic representation in Fig. 1.3, combinations of the therapies are also used in the treatment. The following three procedures are the most basic treatment for a cancer patient. Once the patient is diagnosed with tumor, they are recommended one of the following modalities or their combination.

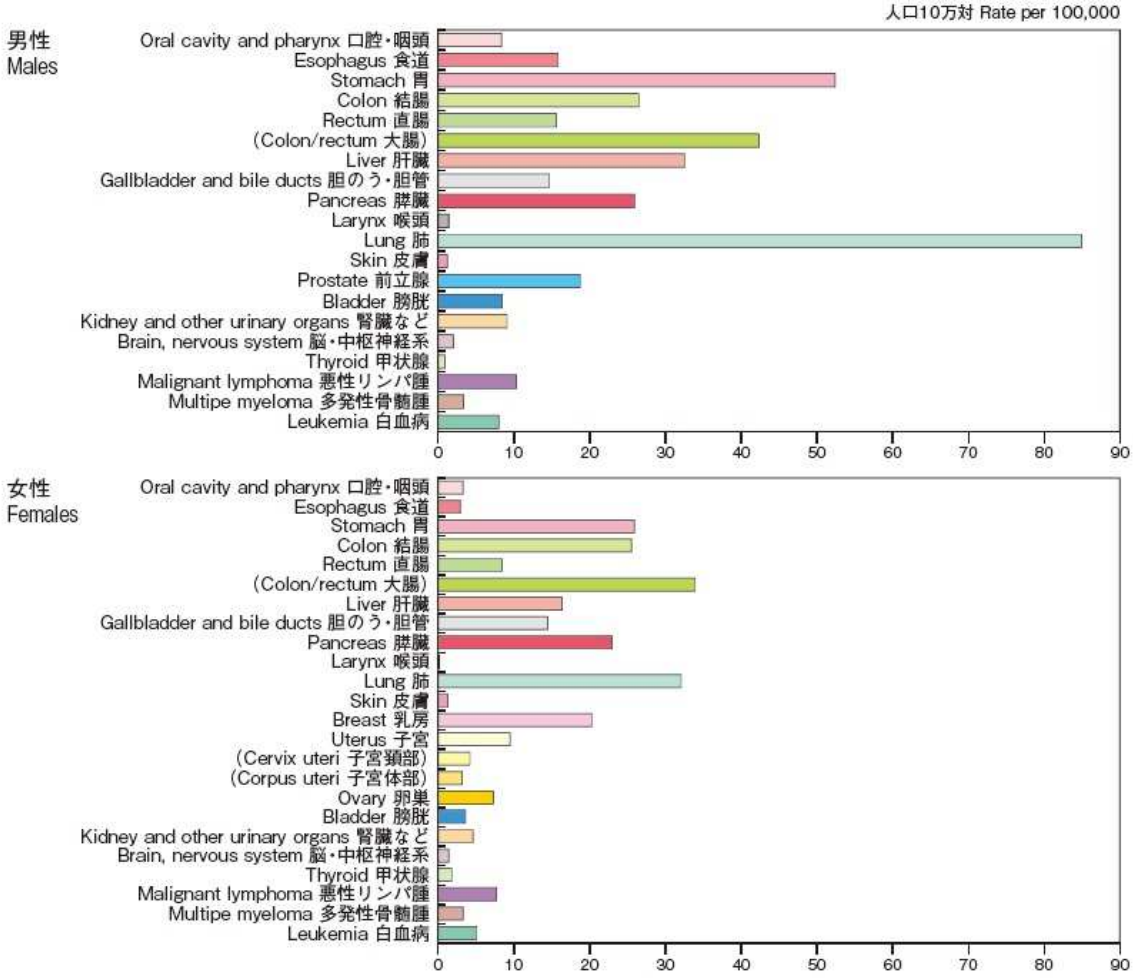

Figure 1.2: Cancer mortality rate for males and females for 2013 in Japan [Ganjoho (2014)].

1.1.1 Surgery

Surgery is one of the common ways of cancer treatment and is most of the time the first possible choice. Surgery is often curative allowing the cancer to stop growing further however it also plays part in diagnosing, staging and supporting the treatment. Surgery is the use of surgical operations in the treatment of cancer. This is generally done by removing the segment or lobe of the organ affected. It is more effective in the early stage when the tumor can be removed completely, without the cancer spreading to the nearby organs.

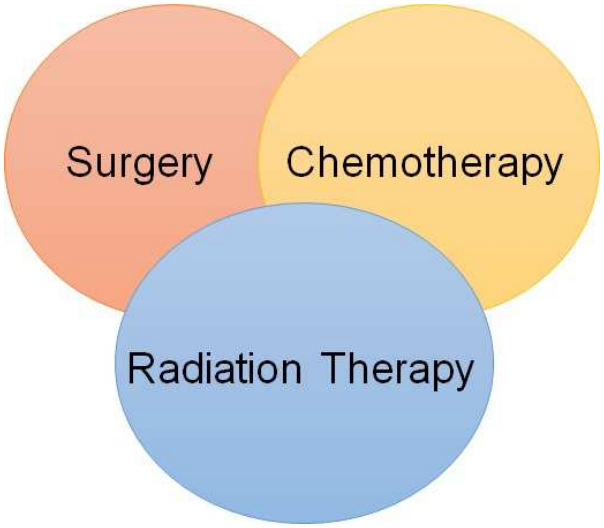

Figure 1.3: Schematic for cancer treatment modalities, used separately or in combination.

1.1.2 Chemotherapy

Chemotherapy is the use of drugs that destroys the cancer cells or prevents cellular replication by interfering with DNA or RNA and vital cellular proteins. Cancer cells divides more frequently compared to other normal cells, hence makes them susceptible to the treatment drugs. Chemotherapy is a systematic treatment i.e. it can kill the cancer cells anywhere in the body. This is always beneficial if there is a spread of cancer beyond the area that cannot be treated by surgery or any other treatment modalities. Chemotherapy can be considered for several reasons such as using it as an adjuvant therapy, to shrink a tumor before surgery, for cure and to improve the symptoms of cancer such as pain etc. As all other modalities, chemotherapy also has its own adverse effects. Since chemotherapy works by interfering with division of cells, it tends to affect those normal cells that divide frequently inducing hair loss, anemia, nausea and many more.

1.1.3 Radiation Therapy

Radiation therapy is a common cancer treatment procedure which uses high energy x-rays or other particles. High energy rays irradiate the tumor and the nearby

lymph nodes causing damages to the DNA in cells which prevents the cell from further division. Cancer cells are most likely to be damaged and will lack the ability to repair. Radiation therapy is also used along with other modalities like surgery or chemotherapy depending upon the type and the stage of the cancer. For example radiation therapy can be used after surgery, to treat the remaining cancer cells and before surgery to decrease the size of the tumor hence making the surgery or chemotherapy treatment more effective. Radiation therapy in general is an external beam radiation therapy which involves the use of external machine for the delivery of high dose radiation. However for lung cancer radiation therapy can also be internal with brachytherapy. In brachytherapy a thin plastic tube is inserted during bronchoscopy and a small amount of radioactive material is passed through the tube delivering the treatment to the precise area. Radiation pneumonitis, esophagitis, dermatitis are some common side effects from radiation therapy.

Radiation therapy for lung being a key part in this research is covered in detail in the following section.

1.2 External beam radiation therapy

External beam radiation therapy (EBRT) is the safe non-invasive procedure for the delivery of radiation beam to the tumor. A linear accelerator focuses the radiation beam to the precise tumor location in lung for a period of time. Modern advancement in computers has led to the advance in imaging technologies used for the treatment planning of radiation therapy. The therapy has improved to a much higher level compared to initial stages when it was based on two dimensional x-ray images and hand calculation. Development in techniques such as computed tomography (CT), magnetic resonance imaging (MRI) and positron emission tomography (PET) has allowed the tumor to be targeted with precision. This development was followed by the development of three dimensional conformal radiation therapy (3D-CRT), intensity modulated radiation therapy (IMRT), and volumetric modulated arc therapy (VMAT) and Image guided radiation

therapy (IGRT) to deliver the radiation dose with pin point accuracy and avoiding the normal tissues using continuous image guidance. Recently, development of stereotactic body radiation therapy (SBRT) has allowed a highly effective treatment in controlling early stage primary tumors.

In the following sections these techniques and the features that separate them with each other will be discussed in detail.

1.2.1 3D-conformal radiation therapy

3D-CRT is a radiation therapy technique in which the treatment is based upon the 3-D anatomic information and using dose distributions that conform as closely as possible to the target with adequate dose to the tumor and minimum dose to the surrounding normal tissue [Khan and Gibbons 2014]. A multi-leaf collimator is generally used to determine the shape and size of the tumor target during the treatment planning.

1.2.2 Intensity modulated radiation therapy

IMRT is a radiation therapy technique in which the beam of non-uniform fluences are delivered to the patient from different direction. This will be optimized in such a way that the high dose will be focused to the tumor, while the critical normal structures getting the minimum dose. It consists of a treatment planning computer system that can calculate the non-uniform fluence maps for multiple beams directed from different directions to maximize the target volume and a computer controlled multileaf collimator (MLC) system which not only helps to shape the beam apertures as in conventional radiation therapy but can be easily programmed for the delivery of IMRT. [Khan and Gibbons 2014].

1.2.3 Volumetric Modulated Arc Therapy

IMRT included a rotational therapy called intensity modulated arc therapy (IMAT). To deliver the intensity modulated field in a particular gantry angle several rotational

arcs with different MLC pattern were required. This several rotations were not considered as a feasible solution in clinical practice. A variation of the technique using a gantry rotation and rapid MLC control was developed to overcome the drawbacks of IMAT, known as VMAT [Otto 2008].

1.2.4 Image guided radiation therapy

Imaging has played a major role in modern radiation therapy. IGRT is a radiation therapy technique that uses advanced imaging techniques to better define the tumor target and beam targeting. It depends upon four major systems for its implementation. The first one is the biological imaging tools for the better definition of tumor volume. The second one is the 4D imaging technique for the modeling the intra-fraction organ motion. Third one is the onboard imaging system registered to the treatment machines for intra-fraction patient localization. One of such onboard imaging system with two X-ray source and detectors with robotic arm. Fourth is the new radiation treatment planning and delivery schemes incorporating the information derived from the new imaging techniques [Xing et al. 2006].

Imaging techniques (kV) that are commercially available these days can be divided into three parts [Yin et al. 2009]:

(i) Radiographic Imaging: This is the most basic imaging technique which acquires 2D projections or planar images. The size of the object imaged depends upon the size of the detector and the distance between the object and the detector.

(ii) Fluoroscopic Imaging: This is the continuous acquisition of images in real-time during the patient setup or registration and the treatment. This allows the real-time monitoring of the system and in this research we use such images for the image prediction system for tracking moving tumors in real-time which is explained in Chapter 2.

(iii) Tomographic Imaging: Many projections can be acquired at different gantry angles allowing the generation of volumetric CT images through various reconstruction methods. Three dimensional volumetric imaging using CT are the latest development

in IGRT field. Helical CT and cone-beam computed tomography (CBCT) are available in different kV imaging systems. CBCT involves multiple kilovolt images which are acquired by using a large flat panel detector [Jaffray et al. 1999].

1.2.5 Stereotactic body radiation therapy

SBRT is an emerging radiation therapy procedure that is highly effective in controlling early stage primary and oligometastatic cancer. The major feature that separates SBRT from conventional treatment is the delivery of large doses in a few fractions which results in a high biological effective dose (BED) [Benedict et al. 2010]. SBRT also minimizes the dose received by the surrounding organs because of the rapid dose fall of gradient encompassing the tumor [Simone et al. 2013]. ELEKTA SBRT system is one of the widely used SBRT system with a x-ray volume imaging (XVI) system and a rotating gantry in which the mega volt (MV) and kilovolt (kV) source are orthogonal to each and other and moves simultaneously. This system also consists of a CBCT integrated into the LINAC as mentioned in section 1.2.4. These CBCT images acquired just prior to the treatment helps to locate the target precisely and to correct the patient positioning [Kida et al. 2012]. The Elekta-synergy system and the XVI unit used in The University of Tokyo Hospital is illustrated in Fig. 1.4

1.2.6 Particle therapy

Apart from the above mentioned therapies, one of the new advancement in radiation therapy is particle therapy. Proton beam therapy is the most common type of particle therapy, which clearly reduces collateral radiation dose to normal tissue when compared with photon (X-ray)-based methods of irradiation and has the potential to selectively and safely escalate dose to high-risk tumors [Merchant and Farr 2014] [Zheng et al. 2015]. Heavy ions such as carbon ions are also been used in the radiation therapy treatment. Carbon ions stopping in the body exhibit a very high Linear Energy Transfer (LET). From this high LET results a very high Relative Biological Efficiency (RBE).

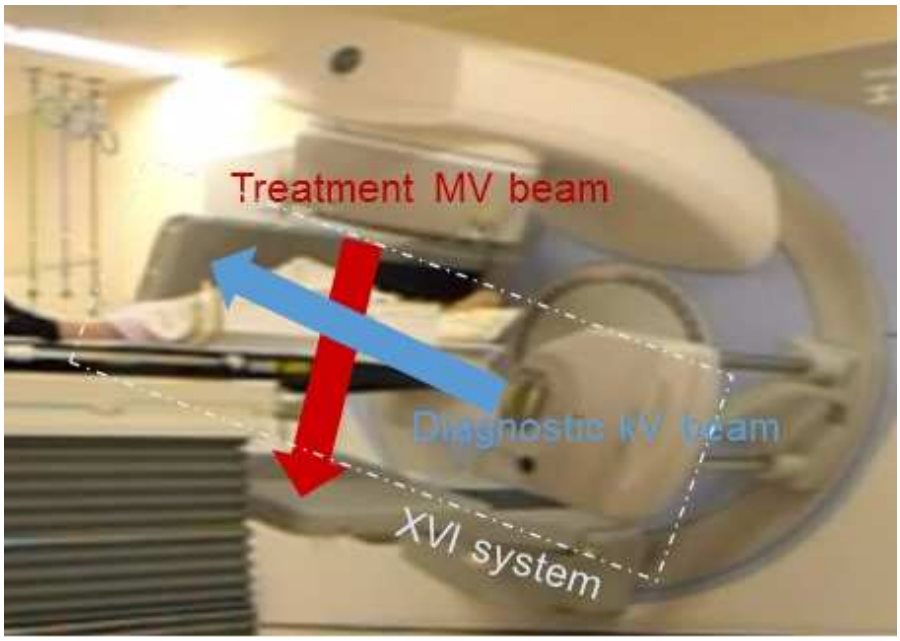

Figure 1.4: Elekta Synergy XVI system for stereotactic body radiation therapy.

This high RBE allows carbon ions to treat efficiently tumors who are radio-resistant and which are difficult to treat with photons or protons [Jongen 2007]. Despite of its advantages compared to the photons, there are several issues with particle therapy such as its cost effectiveness that limits its popularity.

Since this research focuses on lung cancer radiation therapy with photons, it will be explained in the next sections.

1.3 Diagnosis and treatment planning in lung cancer radiation therapy

Imaging plays a major role from the diagnosis, treatment planning to the treatment delivery in lung cancer radiation therapy. Treatment planning is a process that begins with patient data acquisition, planning the dose distribution, analysis of organ at risk (OAR) and also the treatment verification after the delivery. It needs interaction between the radiation oncologists, physicists, dosimetrists, radiation oncologists, radiation therapist. The following block diagram Fig. 1.5 illustrates the process from

diagnosis to treatment in University of Tokyo Hospital, which uses stereotactic beam radiation therapy system from Elekta Synergy shown in Fig. 1.4.

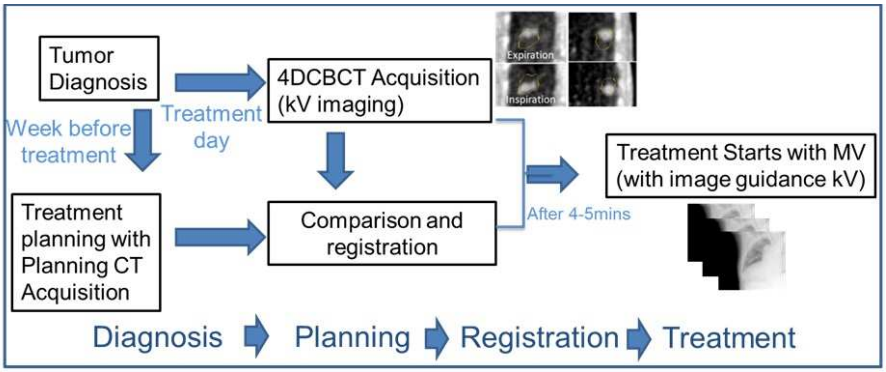

Figure 1.5: Schematic for diagnosis, treatment planning and delivery with Elekta Synergy System.

The recognition of importance of limiting the dose to the normal tissues led to the focus of the treatment to the area where the tumor is actually present or is suspected to be present. Modern day imaging technologies such as CT, MRI and PET gives improved information on target localization resulting in an improved treatment planning [Suetens 2009]. CT images have historically provided the basic information used to define treatment volumes and because they contain information on electron density also forms the basis for calculating three dimensional radiation dose distributions within treatment planning. Introduction of IMRT has improved the definition of the targets and the normal tissues. There are four major target definitions to consider in case of lung tumors.

(i) Gross Tumor Volume (GTV): GTV is the region of tumor. The regions are identified and contoured by the radiation oncologists using a pointing device on individual CT (or MRI) slices. The definition of GTV is of major important step in planning treatment because of all other further planning is dependent upon it.

(ii) Clinical Target Volume (CTV): Once the GTV is delineated, oncologists define the CTV. This takes into account the biological behavior of a specific tumor and allows sufficient margins to account for extension of the disease beyond the imaged tumor boundary.

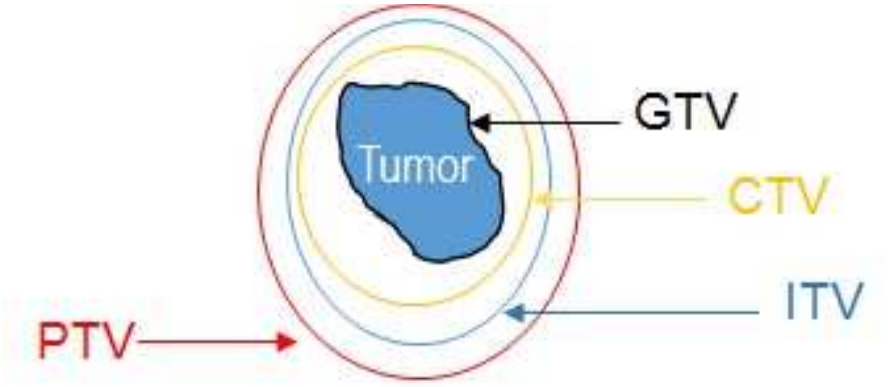

Figure 1.6: Schematic for the distribution of volumes for lung cancer radiation therapy.

(iii) Internal Target Volume (ITV): Lung being a respiratory organ tends to move during the treatment procedure. The internal margin is added to the CTV to compensate for the internal physiological movements and variations in the size, shape and position of CTV during therapy.

(iv) PTV (Planning Target Volume): CTV and ITV is used to generate the PTV, taking into account the effects of patients movement, setup errors that occurs during delivery of radiation (intra-fraction) as well as day to day variation (inter-fraction) [Keall et al. 2006]. So PTV generally consists of CTV, ITV and the set up margin to account for the set up uncertainties. Fig. 1.6 shows the schematic illustration of the distribution volumes used in lung cancer radiation therapy.

1.4 Respiratory motion management in radiation therapy

In radiation therapy, motion is of two main types, the inter-fraction motion that occurs in between the treatment sessions and the intra-fraction motion that is predominantly caused by patient breathing and can affect the treatment outcome of radiation therapy for tumors specially in the thorax and the abdomen region [Bissonnette et al. 2009] [Jiang et al. 2003]. Respiratory motion induces a temporal anatomic changes which distorts the tumor volume (deformation) and the position [Chen et al. 2004]. The example of deformation in pancreatic tumor is illustrated in the four dimensional CT from a patient Fig.1.7 [Hiraoka].

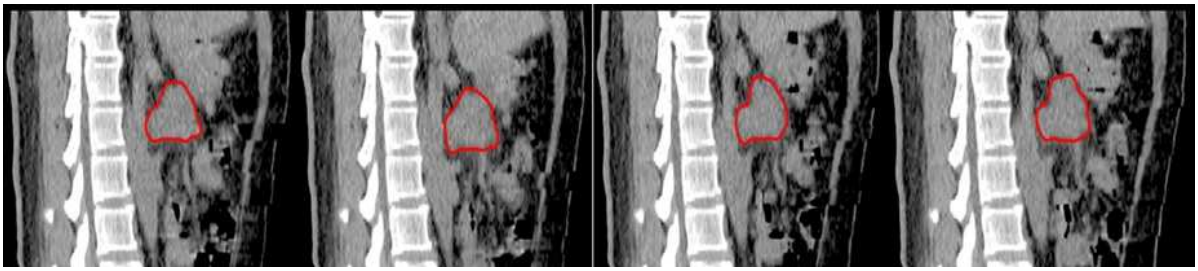

Figure 1.7: Significant deformation in pancreatic tumor due to respiration (time series images).

Lung motion undergoes phenomena called hysteresis resulting a tumor taking different path during exhale and inhale. Such movement compromises the treatment either by reducing the tumor-control probability or increasing the normal tissue toxicity by setting excessively large ITV eventually increasing the PTV as illustrated in the section above.

Tumor motion is complex, heavily depending upon patients and the location of the tumor. Intra-fraction motion can be as large as 5 cm in the superior-inferior (SI) also referred as cranial-caudal (CC) direction [Chen et al. 2001]. In case of anterior-posterior (AP) direction it moves up to 2.4 cm [Shimizu et al. 2001] [Erridge et al. 2003] and up to 1.3 cm for left-right (LR) direction [Ross et al. 1990].

There are several methods that have been developed to reduce the impact of respiratory motion during radiation therapy. One of the commonly used are breath-hold treatment, which is used for lung cancer patient to manage motion [Hanley et al. 1999]. The main objective of this technique is to immobilize the anatomy and minimize the effects of the motion due to breathing. Other management techniques includes motion encompassing methods such as respiratory gating techniques which include gating using fiducial markers, breath hold techniques, forced shallow breathing technique and respiration synchronized techniques. Other than this, real-time tumor tracking is one of the most advanced steps towards the compensation of motion in radiation therapy which is discussed in detail in the following section.

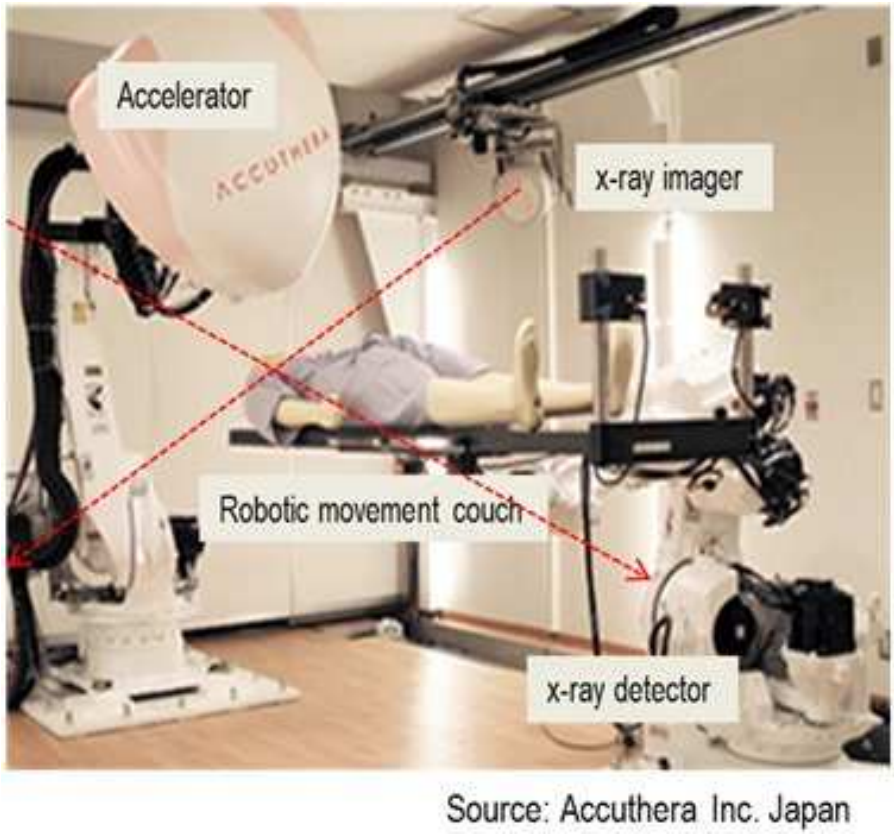

Figure 1.8: Real-time tumor tracking radiation therapy system (Accuthera Inc.).

1.5 Real-time tumor tracking in radiation therapy

Real-time tumor tracking is used to compensate the motion during radiation therapy. It is used to reposition the radiation beam dynamically in order to follow the tumors changing position. This can be done by using a multi-leaf collimator (MLC) or a linear accelerator which is attached to a robotic arm. MLC can change the aperture shape to conform to a deforming tumor projection in the beam eyes view. Alternatively real-time tracking is also accomplished by aligning the tumor to the beam via couch motion. Continuous real-time tracking can remove the need for tumor margin in the dose distribution, maintaining a 100% duty cycle for efficient dose delivery. Fig. 1.8 shows an example of x-ray dynamic tracking therapy system in Accuthera Inc. Japan. An ideal real-time tumor tracking should follow the four basic tasks [Keall et al. 2006] as illustrated below.

1.5.1 Real-time tumor position identification

Identification of tumor position faces the real challenge in real-time tumor tracking. Some popular means for tracking the tumor position includes, real-time imaging of tumor itself via fluoroscopy, real-time imaging of artificial fiducial markers implanted in the tumor, tumor position prediction based on surrogate breathing signals.

1.5.2 Prediction of the tumor motion to compensate time lag

Even with the real-time monitoring of the tumor, the presence of time delay between the beam irradiation and the motion of the target requires the tumor position to be predicted in advance, so that the beam can be synchronized to arrive at the actual position of the tumor once the adjustment have been made.

1.5.3 Reposition of the beam

Beam repositioning is done by using the MLC or the robotic manipulator to move the entire linear accelerator to some degree of freedom. A concern with realigning the beam to the tumor position is that the beam may pass through a sensitive critical structure that was apparently avoided during the CT planning process.

1.5.4 Adapting the dosimetry for breathing effects

The treatment planning imaging study is done to adapt the dosimetry for the breathing effects. The treatment planning imaging study used to calculate the dosimetry captures the anatomy of one static configuration, however during breathing, the anatomy of air volume in the lung are continually changing. This causes the attenuation of treatment beam and changes the relative position of the tumor, normal tissues and critical structures.

1.6 Literature Survey

Respiratory motion management has been a topic of interest for many researchers over the past few years due to which it has received a wide attention in literature. For most types of organ motion there are both intra-fraction and inter-fraction components and that for respiratory motion the magnitude of these two components should be handled carefully [Jiang 2006a] The range of tumor motion varies from 1 to 5 cm in lung, liver and kidneys, depending upon the tumor location and individual patients [Pepin et al. 2011].

Various tumor motion compensation strategies has been investigated and some are still going on. Some advanced motion compensation technique such as beam gating [Jiang 2006b] or beam tracking [Keall et al. 2001] depends upon the precise knowledge of tumor location or position [Cervino et al. 2009]. Some reported methods to determine the tumor location during treatment is direct fluoroscopic tracking [Cui et al. 2007], [Xu et al. 2008], fluoroscopic tracking of implanted fiducial markers [Sharp et al. 2004] [Tang et al. 2007] or deriving tumor positions from external surrogates [Wu et al. 2008].

Fluoroscopic marker-less tracking without any prior imformation are mainly based on template matching method which may fail because of unclear tumor boundary in fluoroscopic images. Using implanted markers suffer from various clinical problems being invasive to patient with a risk of pneumothorax, and also limitation in the number of implanted seed to fully describe the tumor shape variation.

Deriving tumor positions from external surrogates has been implemented clinically for gated lung cancer radiation therapy [Jiang 2006b] however these techniques are accurate only when there is a good correlation between the lung tumor motion and the anatomic surrogate motion. This might not always be true due to the complexity of human breathing. Diaphragm as an anatomic surrogate has also been reported[Cervino et al. 2009] [Mizuguchi et al. 2010] however such study seems to be too much patient specific and depends fully upon the correlation. Non rigid deformation occurs for lung tumors due to the significant tumor mobility and elasticity of lung tissue so surrogate

cannot account for lung tumor shape deformation even if it takes into account the motion [Xu et al. 2007]. Robotic assisted radiation therapy modeling and prediction of lung tumor motion [Ma et al. 2007] have also been reported which widely depends upon the steering of the robotic couch however it is also concerned with the position or motion of the tumor only. The need of consideration of tumor deformation is reported [Xu et al. 2007] using active shape models however it is yet far to be clinically implemented and hugely depends upon the breathing regularity, cardiac motion and a prior knowledge to the tumor shape.

Along with the consideration of tumor motion and tumor shape, real-time consideration becomes absolutely essential. Treatment machines equipped with onboard imaging system with one or two kV x-ray source and detector are used for real-time tracking. This system is referred to as image guided radiation therapy. Even with the implementation of IGRT technique residual intra-fractional motion cannot be completely eliminated [Saw et al. 2007]. It has been reported that it is difficult to localize tumor in 3D space without the use of implanted fiducial markers, or it is lengthy process which cannot be used in real-time [Zeng et al. 2007].

Principal component analysis has been reported of being widely used in the face recognition system [Turk and Pentland 1991] in which few eigen vectors are enough for the recognition of a face. However in case of lungs, lung motion model based on principal component analysis has already been reported [Zhang et al. 2007] [Li et al. 2010] which can efficiently represent lung motion with only a few eigen vectors and coefficients. The PCA lung motion model has a close relationship with the 5D lung motion model [Low et al. 2005] on a theoretical basis. This PCA lung motion model can derive dynamic lung motion with very limited information in accurate way [Zhang et al. 2007]. However these models have been so far used in reconstruction [Li et al. 2010] of the images from the projection images. Prediction of the future images for radiation therapy has not been considered yet.

For tumor tracking, real-time tracking has already been reported [Baroni et al.

2000] [Shimizu et al. 2001] however motion prediction is not sufficient for the accuracy of radiation treatment. Position prediction along with the images might lead to a better accuracy and also the consideration of deformation might spare even the smallest of healthy tissue from irradiation.

Tumor motion and deformation during radiation therapy in case of bladder cancer [Lotz et al. 2006] has been reported. An image registration investigation for the deformation of lung tumors have been reported with some deformation [Wu et al. 2009] however until now it has been neglected reporting it to be too minimal compared to motion. Dynamic tracking of lung deformation, using particle method have been reported [Chhatkuli et al. 2009] in which the simulation result showed that the deformation of lung in SI direction is higher and mostly in the lower part compared to the upper part. The deformation was reported to be from 4 mm to 20 mm depending upon the location at the surface of lung. Since modern day radiation therapy accuracy has been given a major priority hence it becomes necessary to consider the deformation for the pin point accuracy.

As mentioned in Section 1.5.2 using real-time monitoring is not enough to compensate the system specific latencies between the target motion and the beam irradiation. Research shows that for the recently developed systems the delay is 50 ms for Vero SBRT system [Depuydt et al. 2010] 115 ms for the Cyberknife Synchrony system [Seppenwoolde et al. 2007] and about 100 ms for Elekta Synergy System [private communications 2015] due to which the prediction becomes inevitable for the real-time tumor tracking treatment which is the main motivation of this research which will be discussed in the next section.

1.7 Objective of this research

Motion management has been a huge challenge in the field of lung cancer radiation therapy as lung undergoes volumetric expansion and contraction during breathing. Image guidance or IGRT plays a major role when it comes to motion compensation as mentioned in Section 1.2.4. Introduction of dynamic multileaf collimator (DMLC) and real-time tumor tracking in radiation therapy has taken the treatment to a next level. Three dimensional volumetric imaging using computed tomography (CT) mounted on the LINAC represents one of the latest development in the field of IGRT, with four dimensional cone beam CT appearing to be crucial for precise radiation therapy. However some time lag in beam delivery and tumor motion in all the commercially available system somehow hinders the precision of the system. Due to these latencies, prediction becomes a must. Hence real-time tumor tracking with prediction is a major objective of this research.

With real-time tumor tracking being the final goal, the objective is divided into two major parts (i) the development of prediction algorithm using principal component analysis (PCA) and multi-channel singular spectral analysis (MSSA) taking into consideration the robotic couch and the fixed x-ray source and detectors for kV imaging (Fig. 1.8) and (ii) Phase recognition system using priorly obtained cone beam CT for the rotating gantry such as the one used in the University of Tokyo Hospital (Fig. 1.4).

1.8 Outline of this thesis

This thesis consists of four chapters which includes the introduction, material and methods, experimental analysis, results and discussions and finally the conclusion along with the future prospects of this research.

The first chapter includes the general introduction of this research, the background, motivation and literature survey of the current existing technologies have been introduced briefly along with the objective of this research. In the second chapter, the detailed version of the first part of this study i.e. the dynamic image prediction algorithm using PCA and MSSA designed initially for the static gantry radiation therapy system has been introduced. The third chapter details the second part of this study i.e. the real time respiratory phase recognition using the prior 4D-CBCT images. In order to evaluate the feasibility of this study a preliminary study is done to evaluate the time lag of the radiation therapy system which will be explained in this chapter along with the experimental analysis and results.

The last chapter includes a general discussion and conclusion along with the future prospect of the potential of this research for the clinical implementation.

Chapter 2

Part I - Dynamic Image Prediction Using PCA and MSSA

2.1 Introduction to Image Prediction

As introduced in Chapter 1, organ motion due to respiration and setup error uncertainties has been a major challenge in radiation therapy especially for lung cancer with the large amplitude of motion in lungs which is clinically significant [Cervino et al. 2009]. It becomes necessary to confine the radiation to the target and reduce the unnecessary high dose to the healthy tissues for the precise treatment in modern radiation therapy. This has always been a concern for many researchers. In the case of moving tumors like lung, the possible reduction of the internal margin becomes absolutely essential. The PTV for moving tumors must have larger margin compared to the PTV for the static tumor of same CTV. Various strategies have been introduced in order to compensate the tumor motion, beam gating, active or volunteer breath hold, beam tracking, tracking with fiducial or infrared markers etc. [Jiang 2006b]. Long term breath hold technique lacks the patient comfort and beam gating and beam tracking requires a precise knowledge of the position of the tumor [Shirato et al. 2000]. Gating using infrared or implanted markers have been popular treatment lately where the tumor is irradiated during a certain phase. However, there are some disadvantages; a long treatment time due to inefficiency, an uncertainty in the correlation between the target and the marker motion, and invasive procedure for implanted marker [Harada et al. 2002]. Several complications have been reported due to implanted fiducial markers [Bhagat et al. 2010] [Kothary et al. 2009] [Yousefi et al. 2007]. On the other hand, the tumor tracking radiation therapy is currently in applicable phase by means of the development of the image-guidance system. Tracking tumors in real-time has been a topic of interest

for many researchers [Murphy 2004].

A modern IGRT system (explained in Section 1.2.4) has made it possible to monitor the target motion during the external radiation therapy treatment. Most treatment machines are nowadays equipped with one or two kV x-ray source with flat panel detectors [Cho et al. 2010]. Commercially inroom kV imaging systems are divided into three kinds [Yin et al. 2009] i) rail-track mounted systems (ex. Varian GE ExaCTTM system) ii) Ceiling-floor mounted systems (ex. real time tumor tracking radiation therapy system from Accuthera Inc as shown in Fig. 1.8) and (iii) Gantry mounted systems (ex. Elekta Synergy as shown in Fig. 1.4). Sometimes a robotic treatment couch [Ma et al. 2007] are used for the precise radiation delivery. With such systems, the sight of the tumor location can be adjusted based on the real-time x-ray images.

Even with the real time monitoring there exist a time delay between the beam irradiation and the motion of the target. This is mainly because the adaptive response of a radiotherapy system to a tumor position signal cannot occur instantaneously. Hence the beam cannot follow the target accurately [Seppenwoolde et al. 2002]. These are the system latencies which have been mentioned in Chapter 1 Section 1.6. If this time lag is filled with prediction of tumor position then the treatment beam can eventually follow the target.

Predicting the position of the target in advance is considered as an approach to minimize positioning errors due to time lag in the system. The tumor tracking based on prediction of tumor position or motion using implanted or surface markers has already been introduced [Isaksson et al. 2005; Mukumoto et al. 2014]. However, the image prediction would be more direct for the lung tumor such that non-rigid deformation occurs due to the significant tumor mobility and elasticity of lung tissue [Xu et al. 2007]. Also, the predicted image can be used easily to verify the in-treatment accuracy by comparing with planning CT or its digitally reconstructed radiograph. Thus, the image prediction might contribute to the reduction of the internal margin during radiation therapy.

Principal component analysis (PCA) or eigen value analysis is a data feature extraction and data representation technique widely used in data analysis and compression [Turk and Pentland 1991] [Turk et al. 1991]. In cooperation with multi-channel singular spectral analysis (MSSA), this can produce the future data based on the renewal knowledge from moment to moment. Lung motion model based on PCA has already been reported, which efficiently represents lung motion with few principal components [Li et al. 2010] [Li et al. 2011]. On the other hand, these models have so far been used only for the image creation, and prediction has not been considered. In this research we propose a new algorithm for the prediction of lung motion images [Chhatkuli et al. 2015] [Chhatkuli et al. 2012].

First, we examined with a four-dimensional CT (4DCT) image set. The CT image is convenient for the assessment of dynamic image prediction including the information of tumor deformation, however, is not suitable for the real-time prediction because it is currently impossible to acquire the 4DCT images during treatment. Therefore, second, we examined with a kilovolt (kV) fluoroscopic image set, which can be handled in real time.

2.2 Image Prediction algorithm

Image prediction is based on PCA and multi-channel singular spectral analysis (MSSA).

(i) Principal component analysis also known as eigen analysis is a multivariate statistical technique used by many scientific disciplines. It is a technique used for data classification and dimensionality reduction without much loss of information. Information means the variation in the data. It is the way of identifying patterns in the data. After identifying the patterns, PCA allows the compression of data by reducing the number of dimensions without much loss of information. To achieve its goal, PCA computes new variable known as principal components which are obtained by linear combination of the original variables. The first principal component has the largest possible variance.

The second component is computed under the compulsion of being orthogonal to the first component to have the largest possible variation in the data. The main objective of PCA can be classified as follows.

A. Extracting the most important information.

B. Reducing the size of the data by retaining the most important information.

C. Simplification of the description of data

(ii) Multi-channel singular spectral analysis is the generalization of singular spectral analysis (SSA) over time series. SSA combines the elements of classical time series analysis, multivariate statistics, multivariate geometry, dynamical systems and signal processing. It has widely been applied in meteorology and oceanography and climate dynamics field. This method consists in the decomposition of the time series within several components that usually can be identified as trends, oscillatory components or noise components. The SSA algorithm basically depends upon two stages, decomposition and the reconstruction. For the decomposition stage embedding decomposes the original time series data into trajectory matrices and singular value decomposition turns the trajectory matrix into decomposed trajectory matrices which will turn into the trend. The main step in MSSA consists of the construction of the trajectory matrix and its singular value decomposition (SVD).

The image prediction algorithm can be divided into five steps as illustrated in the following sections.

2.2.1 Input image acquisition

For the preliminary study of the image prediction, we employed a 4DCT image set obtained by AcquilionOne^{TM} 320-detector-row CT device (Toshiba). The coronal slices used input images are shown in Fig. 2.1. This set was generated from a lung cancer patient over several breathing cycles. Total 28 CTs which were continuously acquired with the rate of 0.5 sec were taken and were divided into set of training images and testing images in order to verify our prediction algorithm. The voxel size of the CT was

$1mm \times 1mm \times 1mm$. In this study, the 28 images were repeated 5 times in order to increase the number of input data, and then, the last 10 CTs (5 sec) were assigned as the testing images.

For the image prediction, we evaluated the accuracy in the limited view of 4DCT slice referred as large view 4DCT and its region of interest (ROI) i.e. only the tumor and its surrounding area. The pixel size of the large view 4DCT was 140×300 whereas for the ROI, it was 60×52.

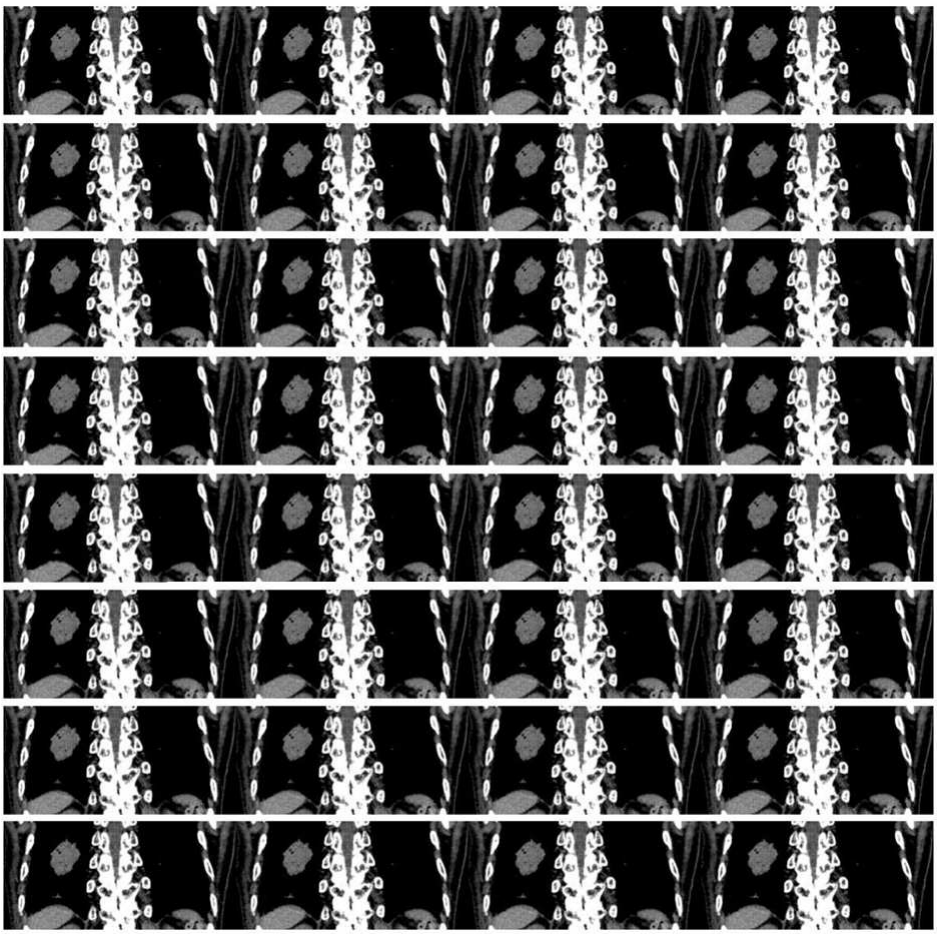

Figure 2.1: 28 reconstructed coronal slice (large view 4DCT) patient images used in the present study.

As second set of input images, kV fluoroscopic images from a linearly driven motion stage phantom were acquired. The phantom and the example of dynamic fluoroscopic images used in this study are illustrated in Figs. 2.2a and 2.2b, respectively. The breathing cycle of the stage was set as 8 sec, and the corresponding amplitude was set as

60 mm. Total 24 images were sequentially acquired and were repeated for 4 cycles. The last 10 images were assigned as testing images similar to the 4DCT images mentioned earlier. The imaging resolution was about 0.2 mm per pixel at the isocenter and the frame rate was 10 frames per sec.

The figure shows a mock tumor marked in red solid circle and the marker marked in blue dotted circle. We attempted two cases for the prediction of kV fluoroscopic images; the ROI from the image shown in Fig. 2.2 with the size 121×323 including the tumor and the marker, and the size 79×174 including only the tumor. These were taken as the input images for the prediction algorithm mentioned in the next Section 2.2.2.

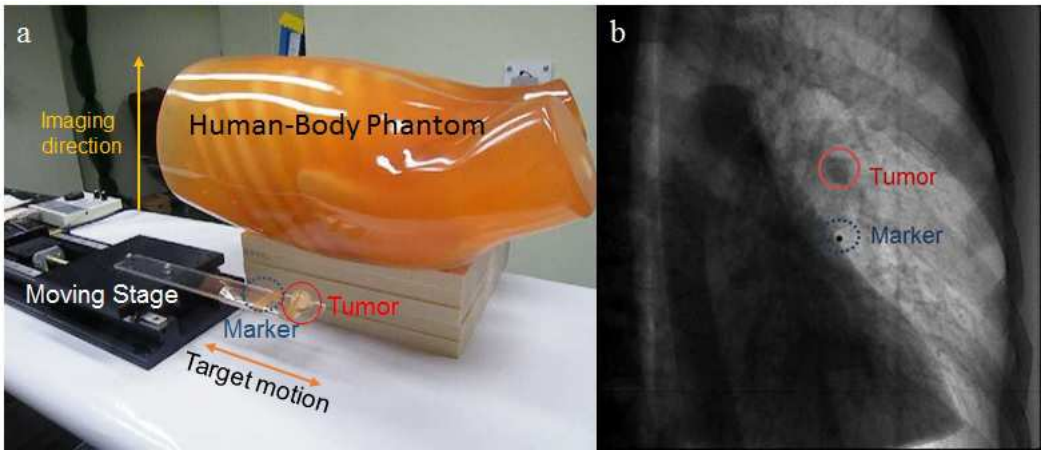

Figure 2.2: a. The human-body and linearly driven motion stage phantom b. Input fluoroscopic image obtained from the phantom.

The algorithm for dynamic image prediction system is divided into three main steps as explained below.

2.2.2 Principal component calculation using PCA

A set of input images with pixel size $w \times h$ are considered. Images are simply two dimensional matrices where the rows and column represents the pixels of the image. Fig. 2.3 shows the representation of one true color (RGB) image in form of a matrix.

In this case we only consider the first plane in the three dimensional array i.e. red. So we transform the matrix to one dimensional vectors (X_1, X_2, ... , X_n) as shown

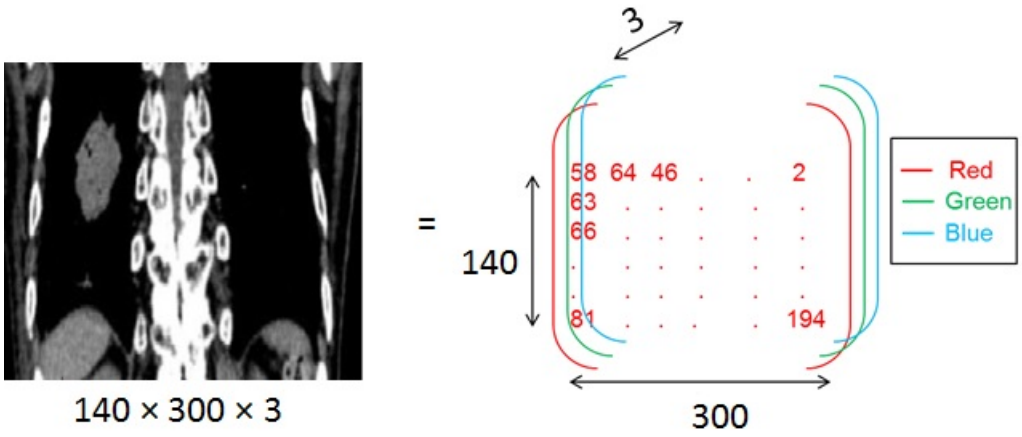

Figure 2.3: Representation of RGB image in form of a matrix.

in Fig. 2.4 where the first image of the time series is transformed to one dimensional matrix.

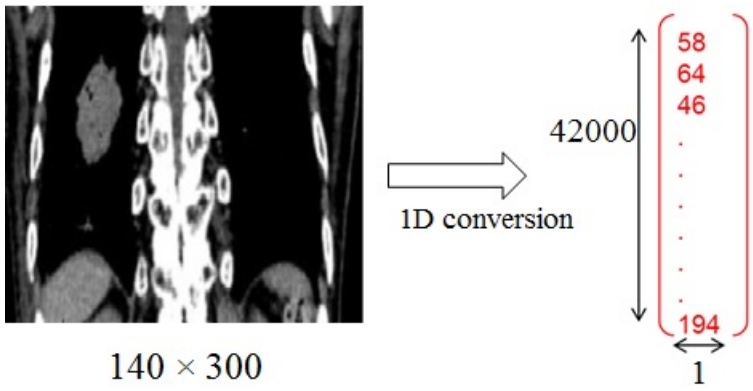

Figure 2.4: Transforming an image to one dimensional matrix.

The 2D input images are converted into 1D image vectors, and then, a single matrix X is constructed by combining (X_1, X_2, ... , X_n) as,

$$X = [X_1, X_2.....X_n], \tag{2.1}$$

where n is the total number of input images for the training set. This is represented by Fig. 2.5, whcih illustrates how the images are transformed into X.

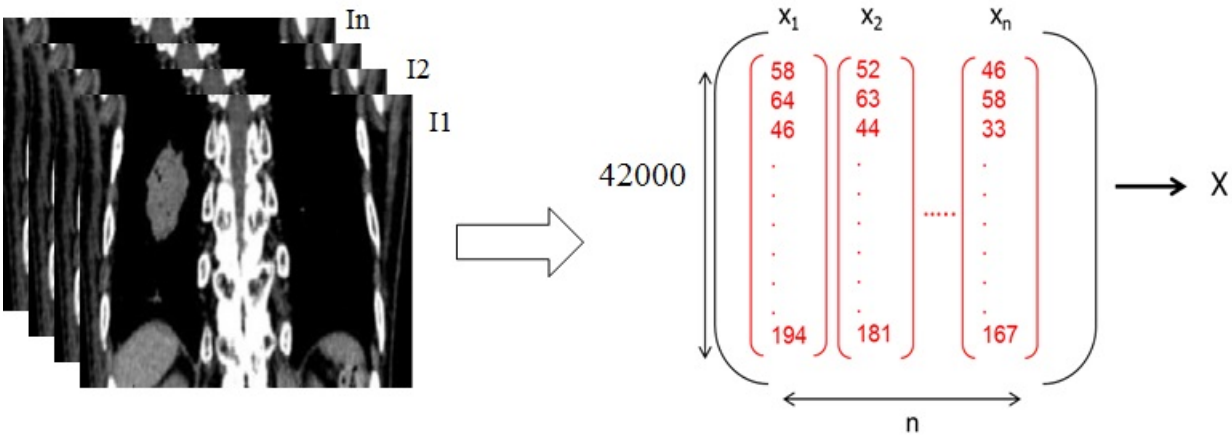

Figure 2.5: Illustration of arrangement of each single matrix into a whole matrix.

Next we calculate the auto-correlation matrix as shown in the Eq. (2.2),

$$Y = XX^T, \tag{2.2}$$

where T refers to transpose. Eigen analysis is then performed on Y resulting,

$$Y\vec{V_i} = \vec{V_i}\lambda_i, \tag{2.3}$$

where $\vec{V_i}$ is the eigen vectors and λ_i is the corresponding eigen value. When transforming the image to 1D image vectors, the resulting image vectors usually lead to a very high dimensional image vector space. This can be minimized by the eigen analysis on X^TX instead where $\vec{v_i}$ is the eigen vector and λ_i is the corresponding eigen value,

$$X^TX\vec{v_i} = \vec{v_i}\lambda_i. \tag{2.4}$$

Multiplying X on both sides, we get,

$$XX^TX\vec{v_i} = X\vec{v_i}\lambda_i, \tag{2.5}$$

and from equation 2.3 and equation 2.5 we can write the following equation,

$$YX\vec{V_i} = XX^TX\vec{v_i} \tag{2.6}$$

which leads to,

$$\vec{V_i} = X\vec{v_i}. \tag{2.7}$$

Eq. (2.7) shows that the dimension of meaningful eigen vectors can only be considered instead of considering the whole matrix. This is real with the very high correlation of consecutive frames in the time series images. The most dominant characteristics of the image are centralized on the highest eigen vector. Hence, in the equation, we setup the number of principal components as number i which denotes the number of eigen vectors. The L eigen vectors V_1 to V_L are then arranged into two dimensional matrices to form the principal component images as explained by the following,

$$X_j = a_{1,j}\vec{V_1} + a_{2,j}\vec{V_2} + \cdots + a_{i,j}\vec{V_i} + \cdots + a_{L,j}\vec{V_L}, \tag{2.8}$$

where $j = (1, 2, ..n)$ and $a_{i,j}$ is the i-th principal coefficient and can be calculated as following,

$$a_{i,j} = X_j\vec{V_i}. \tag{2.9}$$

2.2.3 Coefficient prediction using MSSA

The coefficients calculated from PCA can be used for the prediction of future coefficient estimated by MSSA, which as mentioned earlier is the extended version to multi-dimensions from singular spectral analysis and is useful for analyzing non-linear time series [Mizuguchi et al. 2010]. The coefficients are obtained for the necessity of variation seperation in order to obtain the time dependant data. This time dependant coefficients are further analyzed using MSSA. The time dependant and independant variable can actually be analyzed together however due to the large size of the eigen vectosr it is seperated and only the coefficients are to be considered in MSSA.

The main step of MSSA consists of construction of the trajectory matrix and its

singular value decomposition. We define a trajectory matrix for the coefficients obtained from PCA with time delay matrices as,

$$A_i = \begin{pmatrix} a_{i,M} & a_{i,M+1} & \dots & a_{i,N} \\ a_{i,M-1} & a_{i,M} & \dots & a_{i,N-1} \\ \vdots & \vdots & \ddots & \vdots \\ a_{i,1} & a_{i,2} & \dots & a_{i,N'} \end{pmatrix} (1 \leq i \leq L), \tag{2.10}$$

where arbitrary parameter M is known as the embedded dimension, i is one dimension in L dimensions and N is the number of coefficients using one prediction and N' is $(N - M + 1)$.

The following graph shows the possible representation of the known time series of the coefficients $a_{i,j}$ and the predicted $a_{i,j}$ in the future showing the predicted coefficient after the N time steps.

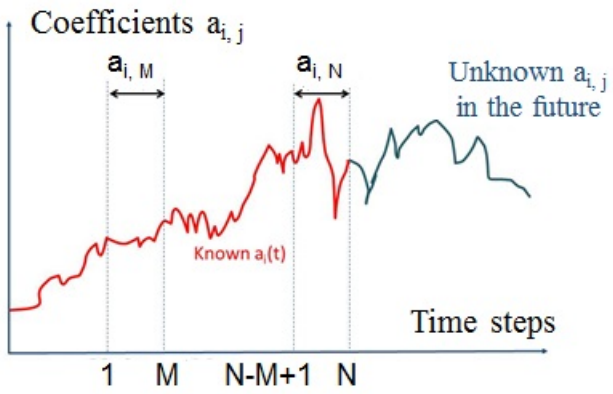

Figure 2.6: Expected representation for the known and the unknown coefficients

The centerized matrix is then obtained in Eq. 2.11 using the difference between all the elements of the trajectory matrix and its mean value.

$$A_i^{cr} = A_i - \frac{1}{N'} \begin{pmatrix} a_{i,M} + a_{i,M+1} + \ldots + a_{i,N} & \ldots & a_{i,M} + a_{i,M+1} + \ldots + a_{i,N} \\ \vdots & \vdots & \vdots \\ a_{i,2} + a_{i,3} + \ldots + a_{i,N'+1} & \ldots & a_{i,2} + a_{i,3} + \ldots + a_{i,N'+1} \\ a_{i,1} + a_{i,2} + \ldots + a_{i,N'} & \ldots & a_{i,1} + a_{i,2} + \ldots + a_{i,N'} \end{pmatrix} \tag{2.11}$$

This Eq.(2.11) can further be denoted as Eq.(2.12),

$$A_i^{cr} = \begin{pmatrix} B_1 & B_2 & \ldots & B_{N'} \end{pmatrix}, \tag{2.12}$$

Auto-correlation matrix is defined with the above trajectory matrix and its transpose as,

$$C_A = AA^T, \tag{2.13}$$

where,

$$A = \begin{pmatrix} a_1^{cr} \\ a_2^{cr} \\ \vdots \\ a_L^{cr} \end{pmatrix}.$$

Eigen analysis is performed as in 2.2.2. We choose r (arbitrary number) largest eigen values and corresponding eigen vectors shown as,

$$E = \begin{pmatrix} E_1 & E_2 & \ldots & E_r \end{pmatrix} \tag{2.14}$$

Using MSSA, we can predict the future data using this E from the equation for principal components of previous time series data. Actually, we create $B_{N'+1}$ matrix by minimizing the follows,

$$(B_{N'+1} - EE^T B_{N'+1})^2 \to min. \tag{2.15}$$

This denotes that $B_{N'+1}$ exists closest to the plane from $(E_1\ E_2 \dots E_r)$. Then $B_{N'+1}$ can be written as,

$$B_{N'+1} = R \begin{pmatrix} a_{1,N+1} \\ a_{2,N+1} \\ \vdots \\ a_{L,N+1} \end{pmatrix} + Q = RP + Q, \tag{2.16}$$

where $P = (a_{1,N+1}, a_{2,N+1}, \cdots, a_{L,N+1})^T$ and Q equals to $B_{N'+1}$ except the unknown component which equals to 0 and R (a $LM \times L$ matrix) components in j row and $(M \times (j-1)+1)$ column $(1 \leq j \leq L)$ are 1 as shown below,

$$R = \begin{pmatrix} 1 & 0 & \dots & 0 \\ 0 & \vdots & \dots & \vdots \\ \vdots & \vdots & \dots & \vdots \\ \vdots & 1 & \dots & \vdots \\ \vdots & 0 & \dots & \vdots \\ \vdots & \vdots & \dots & 1 \\ \vdots & \vdots & \dots & 0 \\ \vdots & \vdots & \dots & \vdots \end{pmatrix} \tag{2.17}$$

According to Eq. (2.15) and Eq. (2.16) we can evaluate P as,

$$P = (I - R^T E E^T R) R^T E E^t Q. \tag{2.18}$$

We can obtain the L unknown future data by solving the condition and setting back the centering values,

$$\begin{pmatrix} a_{1,N+1} \\ a_{2,N+1} \\ \vdots \\ a_{L,N+1} \end{pmatrix} = P + \frac{1}{N'} \begin{pmatrix} a_{1,M} + a_{1,M+1} + \ldots + a_{1,N} \\ a_{2,M} + a_{2,M+1} + \ldots + a_{2,N} \\ \vdots \\ a_{L-1,M} + a_{L-1,M+1} + \ldots + a_{L-1,N} \end{pmatrix} \tag{2.19}$$

2.2.4 Image reformation using PCA

Once the coefficients are predicted, the predicted image can be reformed as an image by multiplying the predicted coefficients and the principal component images. Principal component images are already obtained in 2.2.2 by arranging the eigen vectors to two dimensional matrices. The three principal component images in case of whole 4DCT images are illustrated in Fig. 2.7.

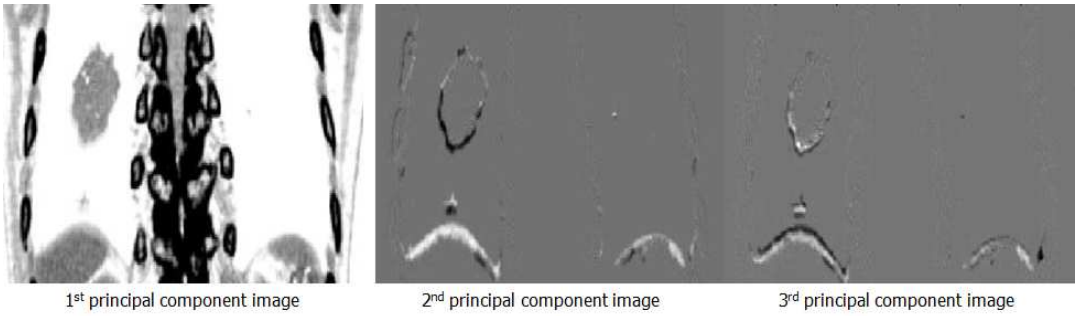

Figure 2.7: Three principal components for large view 4DCT images which are used for reformation of predicted images.

The ten principal components used to reform the images in case of kV images with marker are illustrated in Fig. 2.8.

2.2.5 Quantification using Cross Correlation Coefficient and Structure Similarity Index

To quantify the accuracy of the prediction algorithm two popular index are used to analyze the similarity between the original and the predicted images. The first one is the calculation of cross correlation coefficient calculated as Cor= $\frac{\sum_{i=0}^{N-1}(x_{ori}-x_{av})(y_{pre}-y_{av})}{\sum_{i=0}^{N-1}(x_{ori}-x_{av})^2(y_{prei}-y_{av})^2}$ where x_{ori} is the original image, x_{av} is the average gray level in x_{ori} and similarly y_{pre} is

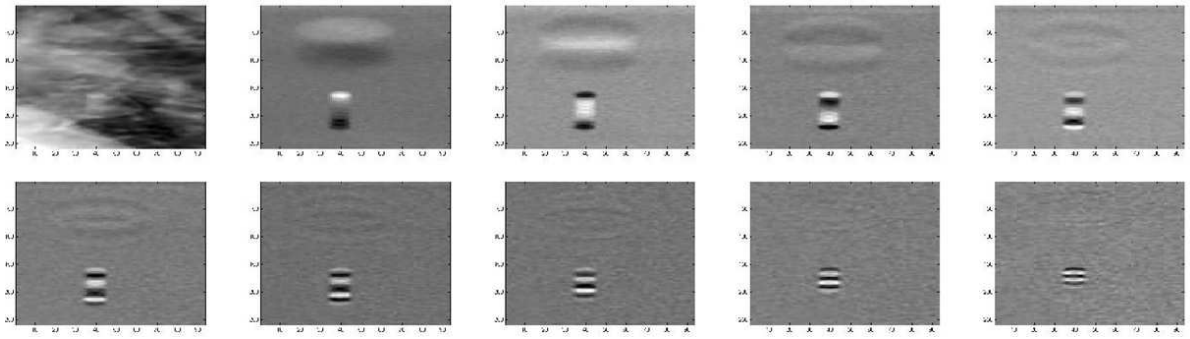

Figure 2.8: Ten principal component images used for the reformation of predicted kV images using markers. (Top row shows the first five principal components and the bottom row shows the last five).

the predicted image and y_{av} is the average gray level in y_{pre}. N is the number of pixel in the image. The quantification is further carried out by analysis the structure similarity index as shown as ssim=$\frac{(2\mu_x\mu_y+c_1)(2\sigma_{xy}+c_2)}{(\mu_x^2+\mu_y^2+c_1)(\sigma_x^2+\sigma_y^2+c_2)}$ where μ_x and μ_y are the average of the original image and the predicted image respectively. σ_x,σ_y and $\sigma_{xy}$are the variance of original, predicted image and their covariance respectvely. c_1 and C_2 are the parameters used for denominator stabilization.

2.3 Results

2.3.1 Results for 4DCT images

I. Large View 4DCT: In 4DCT images, a few principal components were enough to represent the original feature of lung motion and deformation; Fig.2.7 shows the first three principal component images taken in case of large 4DCT images.

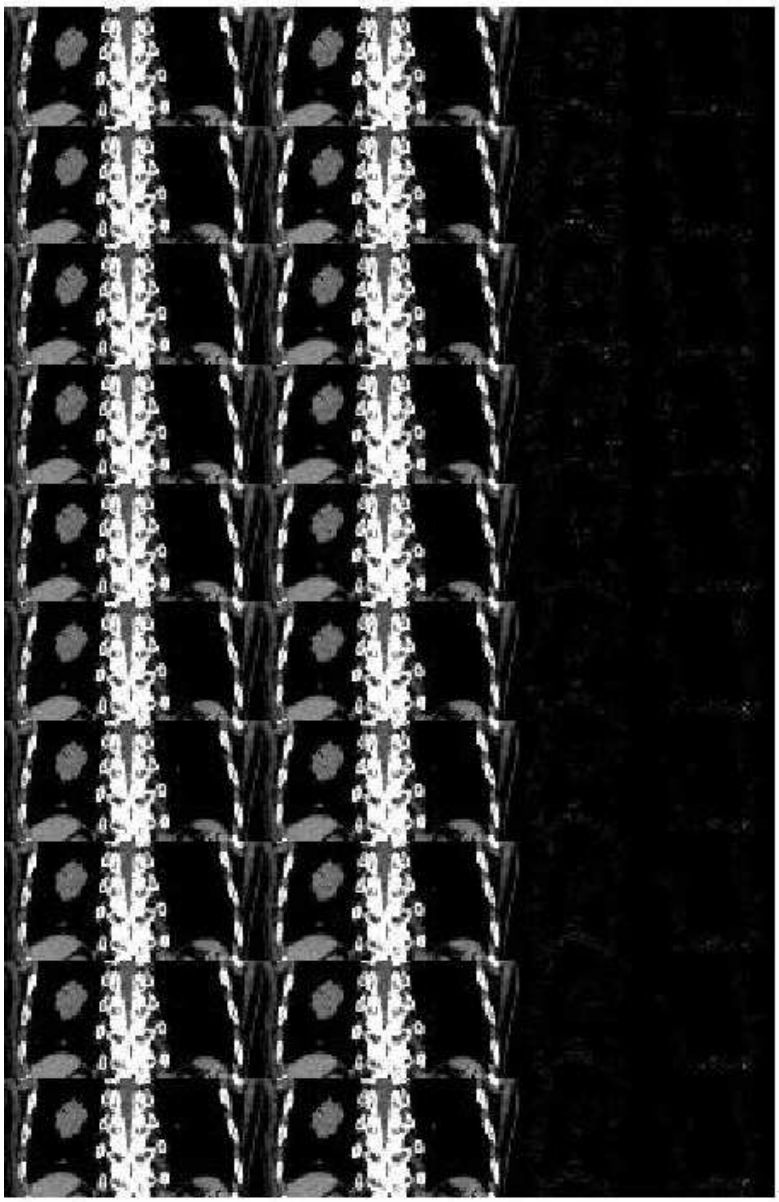

Figure 2.9: Large view 4DCT prediction results for 10 steps representing the original (left column) predicted (center column) and the difference (right column).

One can see that the first principal component represents the entire feature of the lung and the other components give a kind of corrections, especially, in the tumor surface and the diaphragm edge. The prediction results for the ten steps are illustrated in Fig. 2.9 where the left image represents the original image, the bottom represents the predicted image and the right represents the difference between the original and prediction. The difference from the original image is negligibly small, so that the prediction can be successfully obtained with only first three principal components.

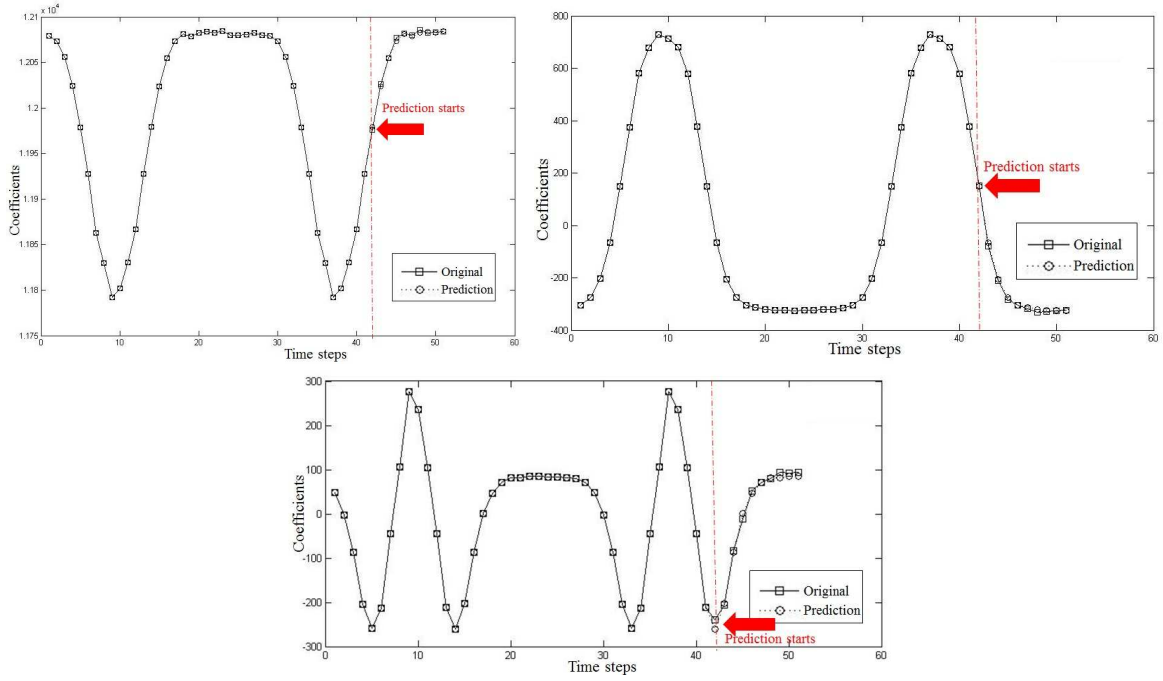

Figure 2.10: Result for the prediction of coefficient for the first principal component (left top), for the second principal component (right top), and for the third principal component (bottom center).

The corresponding coefficient values are indicated in Fig. 2.10 , where the prediction started after the 42^{nd} step for the next ten steps. The predicted coefficient values are in agreement with the original ones. The evaluated image correlation was 0.9998 ± 0.0001 and the SSIM was 0.9953 ± 0.0001 as mentioned in table 2.1.

II. ROI 4DCT:

Similar to the large view 4DCT images, prediction was performed for the tumor region of interest i.e. the maximum anticipated range of the movement of the tumor.

Input Image	Corr. Coef	SSIM	Calc. time
Large 4DCT	0.9998 ± 0.0001	0.9953 ± 0.0001	0.6 sec
ROI 4DCT	0.9992 ± 0.0002	0.9853 ± 0.0001	0.12 sec

Table 2.1: Correlation coefficient, SSIM value and the calculation time for large 4DCT and ROI 4DCT images.

Fig. 2.11 shows the result for the ten steps prediction. The images are predicted with minimum error for the ten further steps. As in case of large 4DCT, three principal components were sufficient for the prediction. The evaluated image cross correlation and SSIM is 0.9992 ± 0.0002 and 0.9853 ± 0.0001 for ROI 4DCT for the ten steps of prediction. This is illustrated in table 2.1

Although the value was slightly superior in large-view 4DCT, the calculation time was reasonably reduced in ROI 4DCT from 0.6 sec to 0.12 sec compared to large 4DCT as mentioned in table 2.1.

2.3.2 Results for kV fluoroscopic images

Similar to the 4DCT images mentioned in section 2.3.1, two different cases were analysed in the kV fluoroscopic images.

I. kV images with the marker: In contrast to 4DCT images, first ten principal components had to be collected for the precise image prediction. Fig. 2.12 shows the prediction result for the kV fluoroscopic images including the marker for the first and the tenth step.

The quantitave analysis of the prediction result using cross correlation and SSIM gave the value 0.9984 ± 0.0017 and 0.9713 ± 0.0001, respectively as shown in table 2.2.

II. kV images without the marker : As mentioned in section 2.2.1, in the second analysis of the kV images, the region of interest was taken in such a way that the marker was not included in the input images. Similar to the marker included case, 10 principal components were enough to predict the image with high precision. In Fig. 2.13 the first and the tenth step of prediction images along with the original and its

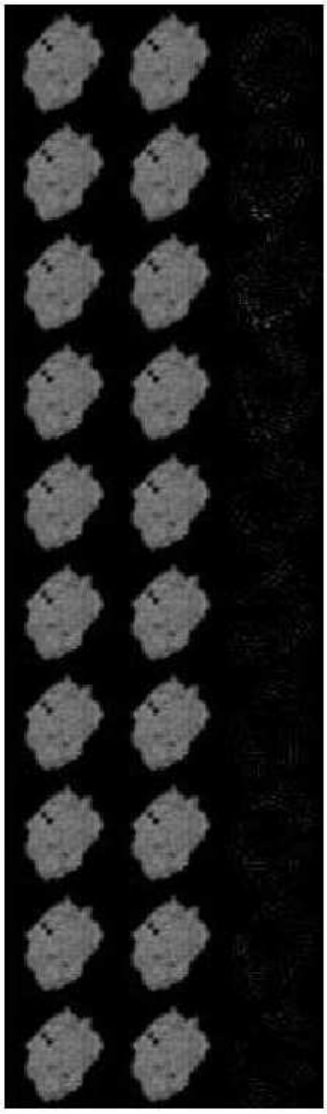

Figure 2.11: 4DCT ROI results from prediction.

difference are illustrated. The cross correlation and SSIM index values were 0.9957 ± 0.0030 and 0.9754 ± 0.004 respectively. The calculation time along with the cross correlation coefficient and SSIM value are mentioned in detail in table 2.2.

The programming environment was MATLAB 2013A. The calculation time was less than 0.6 sec in all cases by using $IntelCore^{TM}$ 2 Duo CPU P880@ 2.66 GHz 4.00 GB RAM. For time improvement and comparison, calculation time is analyzed using CPU Intel Xeon: E 31225 @ 3.10 GHz RAM: 4:00 GB which led to the improvement of the time by 3 times.

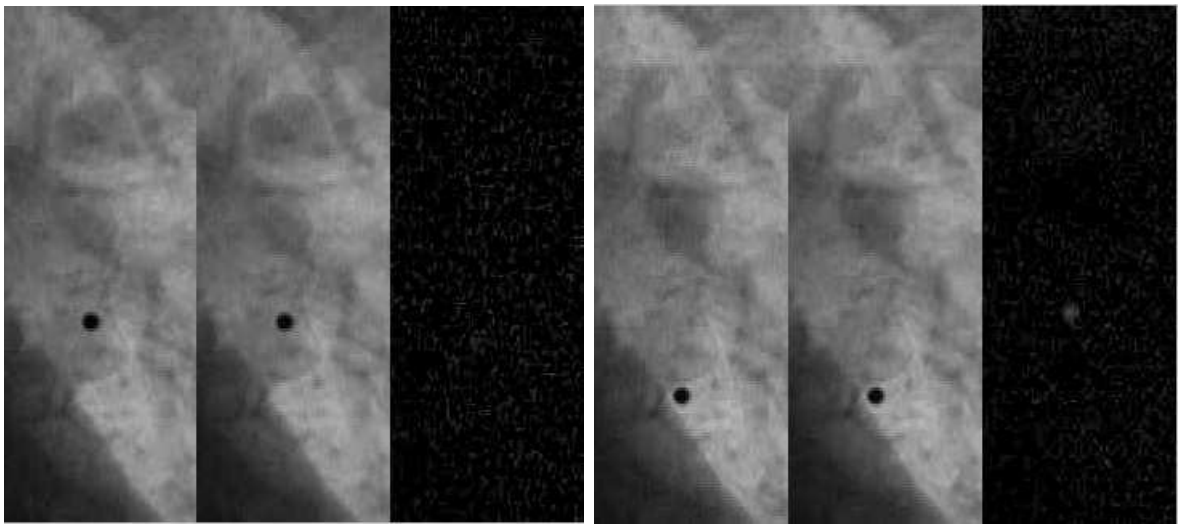

Figure 2.12: Tumor with marker prediction original, prediction and difference for the first (left - first three column) and tenth (right - last three column) prediction steps for the kV fluoroscopic images.

Input Image	Corr. Coef	SSIM	Calc. time
kV(with marker)	0.9984 ± 0.017	0.9713 ± 0.0001	0.53 sec
kV(without marker)	0.9957 ± 0.0030	0.9754 ± 0.004	0.28 sec

Table 2.2: Correlation coefficient, SSIM value and the calculation time for kV images (with and without markers).

2.4 Discussion

This study aims in the development of the prediction algorithm for the possible implementation in image guided lung cancer radiation therapy. To our best knowledge this is the first study which explores the possibility of dynamic tumor tracking with prediction based upon the images. The need of consideration of tumor deformation has been reported using active shape models [Xu et al. 2007], however, it is yet far to be clinically implemented and hugely depends upon the breathing regularity, cardiac motion and a prior knowledge to the tumor shape. The clinically implemented Cyberknife system, the Varian RPM system and the Vero SBRT system includes markers or surface based tracking as an important criteria [Ouzidane et al. 2014]. The potential benefits

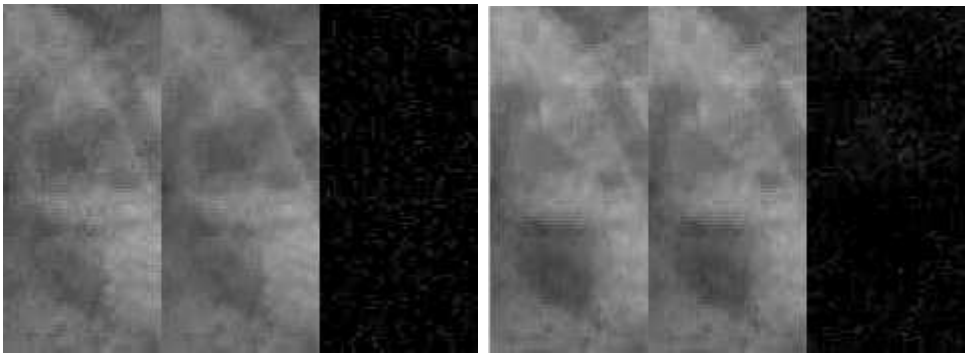

Figure 2.13: Tumor only prediction original, prediction and difference for the first (left- first three column) and tenth (right - last three column) prediction steps for the kV fluoroscopic images.

of our system over other these tumor tracking system includes (1) eliminating the need of implanted or surface markers and (2) ability to consider the deformation of tumor instead of only the motion or position. The phantom images described in Section 2.2.1 did not include the deformation of the tumor, however, from the patient 4DCT images shown in same Section 2.2.1, it was demonstrated that the deformation of the shape of tumor can be successfully predicted in the present algorithm.

It should be noted that the parameter optimization plays a major role in this algorithm. In case of 4DCT images, three eigen vectors were enough to predict and reform. Further increase in the number of eigen vectors did not have noticeable effects on the results. The reshaped eigen vectors (the principal component images) shown in Fig. 2.7 shows that the first principal component covers almost the whole feature of the input image followed by the second and third one after which it becomes minor components. However in the case of kV fluoroscopic images at least seven to ten eigen vectors were required to obtain the significant result. In the present study, we have taken into account the first ten eigen vectors giving the best result. In this case, the actual tumor motion did not have such large cycle and amplitude. It was chosen in order to move the marker and the imitated tumor in various image background (lung, bone and heart), hence the ROI can be further reduced for the small amplitude which ultimately improves the calculating time.

Our input kV fluoroscopic images include both tumor and the marker. It has been already reported the the inter-fractional and intra-fractional variation occurs due to the geometric arrangement from implanted markers [Ueki et al. 2014]. We have shown the prediction result including the marker (tumor and marker) and without the marker (only tumor). In both cases there is no much change in the correlation coefficient but there is significant reduction in time due to the reduction of the image size (smaller ROI) hence this method eliminates the use of considering markers. It can also be seen from the result in Fig. 2.12 that due to characteristics of PCA the difference image is only the minor components that are not considered in the prediction.

In order to evaluate the accuracy of this algorithm the cross correlation and structure similarity index has been calculated. This study is focused mainly upon the ability of tumor tracking with prediction with maximum accuracy and acceptable computing time rather than the computing time alone. This is because of the recent papers reporting the increasing computational power and the possible acceleration using a GPU-based computer [Jia et al. 2014].

The dynamic tracking method using PCA and MSSA was a preliminary study where we tested the accuracy of our algorithm in the patient 4DCT images and kV phantom images. Hence, kV images from the patient data needs to be analyzed next. In that case we can consider the deformation of the tumor and some real breathing pattern as in case of our 4DCT images in Section 2.2.1. Some artifacts and other physical effects are expected which will degrade the quality of image in the patient data. Some preprocessing such as noise removal or image enhancement might be necessary in those cases. We also need to evaluate this algorithm for the projection images in case of the treatment with rotating gantry such as a volumetric modulated arc therapy (VMAT) explained in Section 1.2.3. In the next chapter we explain the tracking in kV projection images but with a different approach.

Bibliography

Amer, A., T. Marchant, J. Sykes, J. Czajka, and C. Moore (2014). Imaging doses from the elekta synergy x-ray cone beam ct system. *The British journal of radiology*.

Baroni, G., G. Ferrigno, R. Orecchia, and A. Pedotti (2000). Real-time three-dimensional motion analysis for patient positioning verification. *Radiotherapy and Oncology 54*(1), 21–27.

Benedict, S. H., K. M. Yenice, D. Followill, J. M. Galvin, W. Hinson, B. Kavanagh, P. Keall, M. Lovelock, S. Meeks, L. Papiez, et al. (2010). Stereotactic body radiation therapy: the report of aapm task group 101. *Medical physics 37*(8), 4078–4101.

Bhagat, N., N. Fidelman, J. C. Durack, J. Collins, R. L. Gordon, J. M. LaBerge, and R. K. Kerlan Jr (2010). Complications associated with the percutaneous insertion of fiducial markers in the thorax. *Cardiovascular and interventional radiology 33*(6), 1186–1191.

Bissonnette, J.-P., K. N. Franks, T. G. Purdie, D. J. Moseley, J.-J. Sonke, D. A. Jaffray, L. A. Dawson, and A. Bezjak (2009). Quantifying interfraction and intrafraction tumor motion in lung stereotactic body radiotherapy using respiration-correlated cone beam computed tomography. *International Journal of Radiation Oncology* Biology* Physics 75*(3), 688–695.

Boge, R., D. Tolbert, and R. Edland (1975). Accessory beam flattening filter for the varian clinac-4 linear accelerator. *Radiology 115*(2), 475–477.

Cervino, L. I., A. K. Chao, A. Sandhu, and S. B. Jiang (2009). The diaphragm as an anatomic surrogate for lung tumor motion. *Physics in medicine and biology 54*(11), 3529.

Chen, G. T., J. H. Kung, and K. P. Beaudette (2004). Artifacts in computed tomography scanning of moving objects. In *Seminars in radiation oncology*, Volume 14, pp. 19–26. Elsevier.

Chen, Q.-S., M. S. Weinhous, F. C. Deibel, J. P. Ciezki, and R. M. Macklis (2001). Fluoroscopic study of tumor motion due to breathing: facilitating precise radiation therapy for lung cancer patients. *Medical physics 28*(9), 1850–1856.

Chhatkuli, R. B., K. Demachi, M. Kawai, H. Sakakibara, and K. Kamiaka (2012). Development of motion image prediction method using principal component analysis.

Chhatkuli, R. B., K. Demachi, N. Miyamoto, M. Uesaka, and A. Haga (2015). Dynamic image prediction using principal component and multi-channel singular spectral analysis: A feasibility study. *Open Journal of Medical Imaging 5*(03), 133.

Chhatkuli, S., S. Koshizuka, and M. Uesaka (2009). Dynamic tracking of lung deformation during breathing by using particle method. *Modelling and Simulation in Engineering 2009*, 7.

Cho, B., P. R. Poulsen, and P. J. Keall (2010). Real-time tumor tracking using sequential kv imaging combined with respiratory monitoring: a general framework applicable to commonly used igrt systems. *Physics in medicine and biology 55*(12), 3299.

Cover, T. M. and J. A. Thomas (1991). Entropy, relative entropy and mutual information. *Elements of Information Theory*, 12–49.

Cui, Y., J. G. Dy, G. C. Sharp, B. Alexander, and S. B. Jiang (2007). Multiple template-based fluoroscopic tracking of lung tumor mass without implanted fiducial markers. *Physics in medicine and biology 52*(20), 6229.

de Koste, J. R. v. S., M. Dahele, H. Mostafavi, A. Sloutsky, S. Senan, B. J. Slotman, and W. F. Verbakel (2015). Markerless tracking of small lung tumors for stereotactic radiotherapy. *Medical physics 42*(4), 1640–1652.

Depuydt, T., O. C. Haas, D. Verellen, S. Erbel, M. De Ridder, and G. Storme (2010). Geometric accuracy evaluation of the new vero stereotactic body radiation therapy system.

Dietrich, L., S. Jetter, T. Tücking, S. Nill, and U. Oelfke (2006). Linac-integrated 4d cone beam ct: first experimental results. *Physics in medicine and biology 51*(11), 2939.

Eisner, R., T. Noever, D. Nowak, W. Carlson, D. Dunn, J. Oates, K. Cloninger, H. Liberman, and R. Patterson (1987). Use of cross-correlation function to detect patient motion during spect imaging. *Journal of nuclear medicine: official publication, Society of Nuclear Medicine 28*(1), 97–101.

Erridge, S. C., Y. Seppenwoolde, S. H. Muller, M. van Herk, K. De Jaeger, J. S. Belderbos, L. J. Boersma, and J. V. Lebesque (2003). Portal imaging to assess set-up errors, tumor motion and tumor shrinkage during conformal radiotherapy of non-small cell lung cancer. *Radiotherapy and Oncology 66*(1), 75–85.

Fu, W., J. Dai, Y. Hu, D. Han, and Y. Song (2004). Delivery time comparison for intensity-modulated radiation therapy with/without flattening filter: a planning study. *Physics in medicine and biology 49*(8), 1535.

Haga, A., S. Kida, N. Saotome, W. Takahashi, H. Yamashita, Y. Masutani, and K. Nakagawa (2015). Others: Four-dimensional cone-beam ct during sbrt. In *Stereotactic Body Radiation Therapy*, pp. 225–236. Springer.

Hanley, J., M. M. Debois, D. Mah, G. S. Mageras, A. Raben, K. Rosenzweig, B. Mychalczak, L. H. Schwartz, P. J. Gloeggler, W. Lutz, et al. (1999). Deep inspiration breath-hold technique for lung tumors: the potential value of target immobilization and reduced lung density in dose escalation. *International Journal of Radiation Oncology* Biology* Physics 45*(3), 603–611.

Hansen, H. H., W. G. Connor, K. Doppke, and M. M. Boone (1972). A new field flattening filter for the clinac-4 1. *Radiology 103*(2), 443–446.

Harada, T., H. Shirato, S. Ogura, S. Oizumi, K. Yamazaki, S. Shimizu, R. Onimaru, K. Miyasaka, M. Nishimura, and H. Dosaka-Akita (2002). Real-time tumor-

tracking radiation therapy for lung carcinoma by the aid of insertion of a gold marker using bronchofiberscopy. *Cancer 95*(8), 1720–1727.

Hiraoka, M. Private Communications.

http://ganjoho.jp/data/, G.

http://www3.jeed.or.jp/gifu/college/, T. P. C.

http://www.enomotoweb.com/, E. B.

Isaksson, M., J. Jalden, and M. J. Murphy (2005). On using an adaptive neural network to predict lung tumor motion during respiration for radiotherapy applications. *Medical physics 32*(12), 3801–3809.

Islam, M. K., T. G. Purdie, B. D. Norrlinger, H. Alasti, D. J. Moseley, M. B. Sharpe, J. H. Siewerdsen, and D. A. Jaffray (2006). Patient dose from kilovoltage cone beam computed tomography imaging in radiation therapy. *Medical physics 33*(6), 1573–1582.

Jaffray, D. A., D. G. Drake, M. Moreau, A. A. Martinez, and J. W. Wong (1999). A radiographic and tomographic imaging system integrated into a medical linear accelerator for localization of bone and soft-tissue targets. *International Journal of Radiation Oncology* Biology* Physics 45*(3), 773–789.

Jaffray, D. A., J. H. Siewerdsen, J. W. Wong, and A. A. Martinez (2002). Flat-panel cone-beam computed tomography for image-guided radiation therapy. *International Journal of Radiation Oncology* Biology* Physics 53*(5), 1337–1349.

Jia, X., P. Ziegenhein, and S. B. Jiang (2014). Gpu-based high-performance computing for radiation therapy. *Physics in medicine and biology 59*(4), R151.

Jiang, S. B. (2006a). Radiotherapy of mobile tumors. In *Seminars in radiation oncology*, Volume 16, pp. 239–248. Elsevier.

Jiang, S. B. (2006b). Technical aspects of image-guided respiration-gated radiation therapy. *Medical Dosimetry 31*(2), 141–151.

Jiang, S. B., C. Pope, K. M. Al Jarrah, J. H. Kung, T. Bortfeld, and G. T. Chen (2003). An experimental investigation on intra-fractional organ motion effects in lung imrt treatments. *Physics in medicine and biology 48*(12), 1773.

Jongen, Y. (2007). Radiotherapy systems using proton and carbon beams. *Bulletin et memoires de l'Academie royale de medecine de Belgique 163*(10-12), 471–8.

Keall, P., V. Kini, S. Vedam, and R. Mohan (2001). Motion adaptive x-ray therapy: a feasibility study. *Physics in Medicine and Biology 46*(1), 1.

Keall, P. J., G. S. Mageras, J. M. Balter, R. S. Emery, K. M. Forster, S. B. Jiang, J. M. Kapatoes, D. A. Low, M. J. Murphy, B. R. Murray, et al. (2006). The management of respiratory motion in radiation oncology report of aapm task group 76a). *Medical physics 33*(10), 3874–3900.

Khan, F. M. and J. P. Gibbons (2014). *Khan's the Physics of Radiation Therapy*. Lippincott Williams & Wilkins.

Kida, S., Y. Masutani, H. Yamashita, T. Imae, T. Matsuura, N. Saotome, K. Ohtomo, K. Nakagawa, and A. Haga (2012). In-treatment 4d cone-beam ct with image-based respiratory phase recognition. *Radiological physics and technology 5*(2), 138–147.

Kothary, N., J. J. Heit, J. D. Louie, W. T. Kuo, B. W. Loo, A. Koong, D. T. Chang, D. Hovsepian, D. Y. Sze, and L. V. Hofmann (2009). Safety and efficacy of percutaneous fiducial marker implantation for image-guided radiation therapy. *Journal of Vascular and Interventional Radiology 20*(2), 235–239.

Li, R., X. Jia, J. H. Lewis, X. Gu, M. Folkerts, C. Men, and S. B. Jiang (2010). Real-time volumetric image reconstruction and 3d tumor localization based on a single x-ray projection image for lung cancer radiotherapy. *Medical physics 37*(6), 2822–2826.

Li, R., J. H. Lewis, X. Jia, T. Zhao, W. Liu, S. Wuenschel, J. Lamb, D. Yang, D. A. Low, and S. B. Jiang (2011). On a pca-based lung motion model. *Physics in medicine and biology 56*(18), 6009.

Li, T., L. Xing, P. Munro, C. McGuinness, M. Chao, Y. Yang, B. Loo, and A. Koong (2006). Four-dimensional cone-beam computed tomography using an on-board imager. *Medical physics 33*(10), 3825–3833.

Lotz, H. T., F. J. Pos, M. C. Hulshof, M. van Herk, J. V. Lebesque, J. C. Duppen, and P. Remeijer (2006). Tumor motion and deformation during external radiotherapy of bladder cancer. *International Journal of Radiation Oncology* Biology* Physics 64*(5), 1551–1558.

Low, D. A., P. J. Parikh, W. Lu, J. F. Dempsey, S. H. Wahab, J. P. Hubenschmidt, M. M. Nystrom, M. Handoko, and J. D. Bradley (2005). Novel breathing motion model for radiotherapy. *International Journal of Radiation Oncology* Biology* Physics 63*(3), 921–929.

Ma, L., C. Herrmann, and K. Schilling (2007). Modeling and prediction of lung tumor motion for robotic assisted radiotherapy. In *Intelligent Robots and Systems, 2007. IROS 2007. IEEE/RSJ International Conference on*, pp. 189–194. IEEE.

Maes, F., D. Vandermeulen, and P. Suetens (2003). Medical image registration using mutual information. *Proceedings of the IEEE 91*(10), 1699–1722.

Merchant, T. E. and J. B. Farr (2014). Proton beam therapy: A fad or a new standard of care. *Current opinion in pediatrics 26*(1), 3–8.

Miyamoto, N., M. Ishikawa, K. Sutherland, R. Suzuki, T. Matsuura, C. Toramatsu, S. Takao, H. Nihongi, S. Shimizu, K. Umegaki, et al. (2015). A motion-compensated image filter for low-dose fluoroscopy in a real-time tumor-tracking radiotherapy system. *Journal of radiation research 56*(1), 186–196.

Mizuguchi, A., K. Demachi, and M. Uesaka (2010). Establish of the prediction system of chest skin motion with ssa method. *International Journal of Applied Electromagnetics and Mechanics 33*(3, 4).

Mukumoto, N., M. Nakamura, M. Yamada, K. Takahashi, H. Tanabe, S. Yano, Y. Miyabe, N. Ueki, S. Kaneko, Y. Matsuo, et al. (2014). Intrafractional track-

ing accuracy in infrared marker-based hybrid dynamic tumour-tracking irradiation with a gimballed linac. *Radiotherapy and Oncology*.

Murphy, M. J. (2004). Tracking moving organs in real time. In *Seminars in radiation oncology*, Volume 14, pp. 91–100. Elsevier.

Murphy, M. J., J. Balter, S. Balter, J. A. BenComo Jr, I. J. Das, S. B. Jiang, C.-M. Ma, G. H. Olivera, R. F. Rodebaugh, K. J. Ruchala, et al. (2007). The management of imaging dose during image-guided radiotherapy: report of the aapm task group 75. *Medical physics 34*(10), 4041–4063.

Nakagawa, K., A. Haga, S. Kida, Y. Masutani, H. Yamashita, W. Takahashi, A. Sakumi, N. Saotome, T. Shiraki, K. Ohtomo, et al. (2012). 4d registration and 4d verification of lung tumor position for stereotactic volumetric modulated arc therapy using respiratory-correlated cone-beam ct. *Journal of radiation research*, rrs058.

Nakagawa, K., A. Haga, A. Sakumi, H. Yamashita, H. Igaki, T. Shiraki, K. Ohtomo, Y. Iwai, and K. Yoda (2014). Impact of flattening-filter-free techniques on delivery time for lung stereotactic volumetric modulated arc therapy and image quality of concurrent kilovoltage cone-beam computed tomography: a preliminary phantom study. *Journal of radiation research 55*(1), 200–202.

Nakagawa, K., S. Kida, A. Haga, Y. Masutani, H. Yamashita, T. Imae, K. Tanaka, K. Ohtomo, Y. Iwai, and K. Yoda (2011). Cone beam computed tomography data acquisition during vmat delivery with subsequent respiratory phase sorting based on projection image cross-correlation. *Journal of radiation research 52*(1), 112–113.

OBrien, P., B. Gillies, M. Schwartz, C. Young, and P. Davey (1991). Radiosurgery with unflattened 6-mv photon beams. *Medical physics 18*(3), 519–521.

Otto, K. (2008). Volumetric modulated arc therapy: Imrt in a single gantry arc. *Medical physics 35*(1), 310–317.

Ouzidane, M., J. Evans, and T. Djemil (2014). Dedicated linear accelerators for stereotactic radiation therapy. In S.H.Benedict, D.J.Schlesinger, S.J.Goetsch, and B.D.Kavanagh (Eds.), *Sterotactic Radiosurgery and Stereotactic Body Radiation Therapy*. Boca Raton, FL 33487-2742: CRC Press, Taylor and Francis Group.

Park, J. C., J. S. Kim, S. H. Park, M. J. Webster, S. Lee, W. Y. Song, and Y. Han (2014). Four dimensional digital tomosynthesis using on-board imager for the verification of respiratory motion. *PloS one 9*(12), e115795.

Pepin, E. W., H. Wu, and H. Shirato (2011). Dynamic gating window for compensation of baseline shift in respiratory-gated radiation therapy. *Medical physics 38*(4), 1912–1918.

Perkins, C. L., T. Fox, E. Elder, D. A. Kooby, C. Staley 3rd, and J. Landry (2006). Image-guided radiation therapy (igrt) in gastrointestinal tumors. *Jop 7*(4), 372–381.

Pluim, J. P., J. A. Maintz, M. Viergever, et al. (2003). Mutual-information-based registration of medical images: a survey. *Medical Imaging, IEEE Transactions on 22*(8), 986–1004.

Rao, Y. R., N. Prathapani, and E. Nagabhooshanam. Application of normalized cross correlation to image registration.

Ross, C. S., D. H. Hussey, E. C. Pennington, W. Stanford, and J. F. Doornbos (1990). Analysis of movement of intrathoracic neoplasms using ultrafast computerized tomography. *International Journal of Radiation Oncology* Biology* Physics 18*(3), 671–677.

Sarvaiya, J. N., S. Patnaik, and S. Bombaywala (2009). Image registration by template matching using normalized cross-correlation. In *Advances in Computing, Control, & Telecommunication Technologies, 2009. ACT'09. International Conference on*, pp. 819–822. IEEE.

Saunders, J. K., D. Graves, and G. Scarth (2012, October 23). Mri guided radiation therapy. US Patent 8,295,906.

Saw, C., E. Brandner, R. Selvaraj, H. Chen, M. S. Huq, and D. Heron (2007). A review on the clinical implementation of respiratory-gated radiation therapy. *Biomedical imaging and intervention journal 3*(1).

Seppenwoolde, Y., R. I. Berbeco, S. Nishioka, H. Shirato, and B. Heijmen (2007). Accuracy of tumor motion compensation algorithm from a robotic respiratory tracking system: a simulation study. *Medical physics 34*(7), 2774–2784.

Seppenwoolde, Y., H. Shirato, K. Kitamura, S. Shimizu, M. van Herk, J. V. Lebesque, and K. Miyasaka (2002). Precise and real-time measurement of 3d tumor motion in lung due to breathing and heartbeat, measured during radiotherapy. *International Journal of Radiation Oncology* Biology* Physics 53*(4), 822–834.

Sharp, G. C., S. B. Jiang, S. Shimizu, and H. Shirato (2004). Tracking errors in a prototype real-time tumour tracking system. *Physics in medicine and biology 49*(23), 5347.

Shimizu, S., H. Shirato, S. Ogura, H. Akita-Dosaka, K. Kitamura, T. Nishioka, K. Kagei, M. Nishimura, and K. Miyasaka (2001). Detection of lung tumor movement in real-time tumor-tracking radiotherapy. *International Journal of Radiation Oncology* Biology* Physics 51*(2), 304–310.

Shirato, H., S. Shimizu, T. Kunieda, K. Kitamura, M. van Herk, K. Kagei, T. Nishioka, S. Hashimoto, K. Fujita, H. Aoyama, et al. (2000). Physical aspects of a real-time tumor-tracking system for gated radiotherapy. *International Journal of Radiation Oncology* Biology* Physics 48*(4), 1187–1195.

Simone, C. B., B. Wildt, A. R. Haas, G. Pope, R. Rengan, and S. M. Hahn (2013). Stereotactic body radiation therapy for lung cancer. *CHEST Journal 143*(6), 1784–1790.

Sonke, J., P. Remeijer, and M. van Herk (2010). Four dimensional cone beam ct acquisition concurrent with vmat delivery. *Radiother Oncol 96*(Suppl 1), S75.

Sonke, J.-J., L. Zijp, P. Remeijer, and M. van Herk (2005). Respiratory correlated cone beam ct. *Medical physics 32*(4), 1176–1186.

Suetens, P. (2009). *Fundamentals of medical imaging*. Cambridge university press.

Tang, X., G. C. Sharp, and S. B. Jiang (2007). Fluoroscopic tracking of multiple implanted fiducial markers using multiple object tracking. *Physics in medicine and biology 52*(14), 4081.

Teske, H., P. Mercea, M. Schwarz, N. H. Nicolay, F. Sterzing, and R. Bendl (2015). Real-time markerless lung tumor tracking in fluoroscopic video: Handling overlapping of projected structures. *Medical physics 42*(5), 2540–2549.

Thomas, E. M., R. A. Popple, B. M. Prendergast, G. M. Clark, M. C. Dobelbower, and J. B. Fiveash (2013). Effects of flattening filter-free and volumetric-modulated arc therapy delivery on treatment efficiency. *Journal of Applied Clinical Medical Physics 14*(6).

Turk, M. and A. Pentland (1991). Eigenfaces for recognition. *Journal of cognitive neuroscience 3*(1), 71–86.

Turk, M., A. P. Pentland, et al. (1991). Face recognition using eigenfaces. In *Computer Vision and Pattern Recognition, 1991. Proceedings CVPR'91., IEEE Computer Society Conference on*, pp. 586–591. IEEE.

Ueki, N., Y. Matsuo, M. Nakamura, N. Mukumoto, Y. Iizuka, Y. Miyabe, A. Sawada, T. Mizowaki, M. Kokubo, and M. Hiraoka (2014). Intra-and interfractional variations in geometric arrangement between lung tumours and implanted markers. *Radiotherapy and Oncology 110*(3), 523–528.

Vassiliev, O. N., S. F. Kry, J. Y. Chang, P. A. Balter, U. Titt, and R. Mohan (2009). Stereotactic radiotherapy for lung cancer using a flattening filter free clinac. *Journal of Applied Clinical Medical Physics 10*(1).

Wolthaus, J. W., C. Schneider, J.-J. Sonke, M. van Herk, J. S. Belderbos, M. M. Rossi, J. V. Lebesque, and E. M. Damen (2006). Mid-ventilation ct scan construction from four-dimensional respiration-correlated ct scans for radiotherapy planning of lung cancer patients. *International Journal of Radiation Oncology* Biology* Physics 65*(5), 1560–1571.

Wooten, H. O., V. Rodriguez, O. Green, R. Kashani, L. Santanam, K. Tanderup, S. Mutic, and H. H. Li (2015). Benchmark imrt evaluation of a co-60 mri-guided radiation therapy system. *Radiotherapy and Oncology 114*(3), 402–405.

Wu, H., Q. Zhao, R. I. Berbeco, S. Nishioka, H. Shirato, and S. B. Jiang (2008). Gating based on internal/external signals with dynamic correlation updates. *Physics in medicine and biology 53*(24), 7137.

Wu, J., P. Lei, R. Shekhar, H. Li, M. Suntharalingam, and W. D. D'Souza (2009). Do tumors in the lung deform during normal respiration? an image registration investigation. *International Journal of Radiation Oncology* Biology* Physics 75*(1), 268–275.

Xing, L., B. Thorndyke, E. Schreibmann, Y. Yang, T.-F. Li, G.-Y. Kim, G. Luxton, and A. Koong (2006). Overview of image-guided radiation therapy. *Medical Dosimetry 31*(2), 91–112.

Xu, Q., R. J. Hamilton, R. A. Schowengerdt, B. Alexander, and S. B. Jiang (2008). Lung tumor tracking in fluoroscopic video based on optical flow. *Medical physics 35*(12), 5351–5359.

Xu, Q., R. J. Hamilton, R. A. Schowengerdt, and S. B. Jiang (2007). A deformable lung tumor tracking method in fluoroscopic video using active shape models: a feasibility study. *Physics in medicine and biology 52*(17), 5277.

Yamashita, H., A. Haga, W. Takahashi, R. Takenaka, T. Imae, S. Takenaka, and K. Nakagawa (2014). Volumetric modulated arc therapy for lung stereotactic radiation therapy can achieve high local control rates. *Radiat Oncol 9*, 243.

Yin, F., J. Wong, J. Balter, S. Benedict, J. Bissonnette, T. Craig, L. Dong, D. Jaffray, S. Jiang, S. Kim, et al. (2009). The role of in-room kv x-ray imaging for patient setup and target localization: Report of aapm task group 104. *AAPM Report (American Association of Physicists in Medicine, College Park, MD, 2009)*, 62.

Yousefi, S., B. T. Collins, C. A. Reichner, E. D. Anderson, C. Jamis-Dow, G. Gagnon, S. Malik, B. Marshall, T. Chang, and F. Banovac (2007). Complications of thoracic computed tomography–guided fiducial placement for the purpose of stereotactic body radiation therapy. *Clinical lung cancer 8*(4), 252–256.

Zeng, R., J. Fessler, J. M. Balter, et al. (2007). Estimating 3-d respiratory motion from orbiting views by tomographic image registration. *Medical Imaging, IEEE Transactions on 26*(2), 153–163.

Zhang, Q., A. Pevsner, A. Hertanto, Y.-C. Hu, K. E. Rosenzweig, C. C. Ling, and G. S. Mageras (2007). A patient-specific respiratory model of anatomical motion for radiation treatment planning. *Medical Physics 34*(12), 4772–4781.

Zhang, X., N. Homma, K. Ichiji, M. Abe, N. Sugita, Y. Takai, Y. Narita, and M. Yoshizawa (2014). A kernel-based method for markerless tumor tracking in kv fluoroscopic images. *Physics in medicine and biology 59*(17), 4897.

Zheng, Y., H. Singh, L. Zhao, E. Ramirez, S. Rana, K. Prabhu, L. Doh, and G. Larson (2015). Adaptive radiation therapy for lung cancer using uniform scanning proton beams: Adaptation strategies, practical considerations, and clinical outcomes. *International Journal of Radiation Oncology* Biology* Physics 93*(3), S29.

Zijp, L., J.-J. Sonke, and M. van Herk (2004). Extraction of the respiratory signal from sequential thorax cone-beam x-ray images. In *ICCR*.

APPENDIX A

Principal Component Evaluation

A.1 Considering the minor components

It has been mentioned in Chapter 2 that optimization of the parameters, especially the number of principal component plays a major role in the algorithm. So far, only the major components are considered. It is quite clear that theoretically more the minor principal components are considered more will be the accuracy in prediction as images can be reformed using more number of components. However, the analysis below showed a different results in both the kV and the 4DCT case.

A.1.1 Minor components in kV images

Fig. A.1 shows the image prediction result using PCA and MSSA, the left image shows the original image, middle image shows the prediction image and the right image show the difference between the original and the predicted ones.

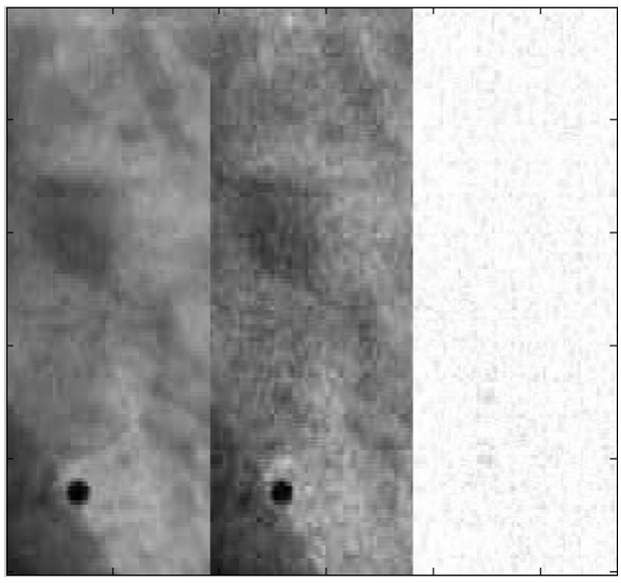

Figure A.1: Prediction results, original (left), prediction (middle) and difference (right) using 38 component for kV image.

The predicted image (middle) shows some blurring, in order to analyze the result each principal component is checked one by one. Fig. A.2 shows the 38 principal component images where we can see after the 10th component, principal component shows the increase in noise.

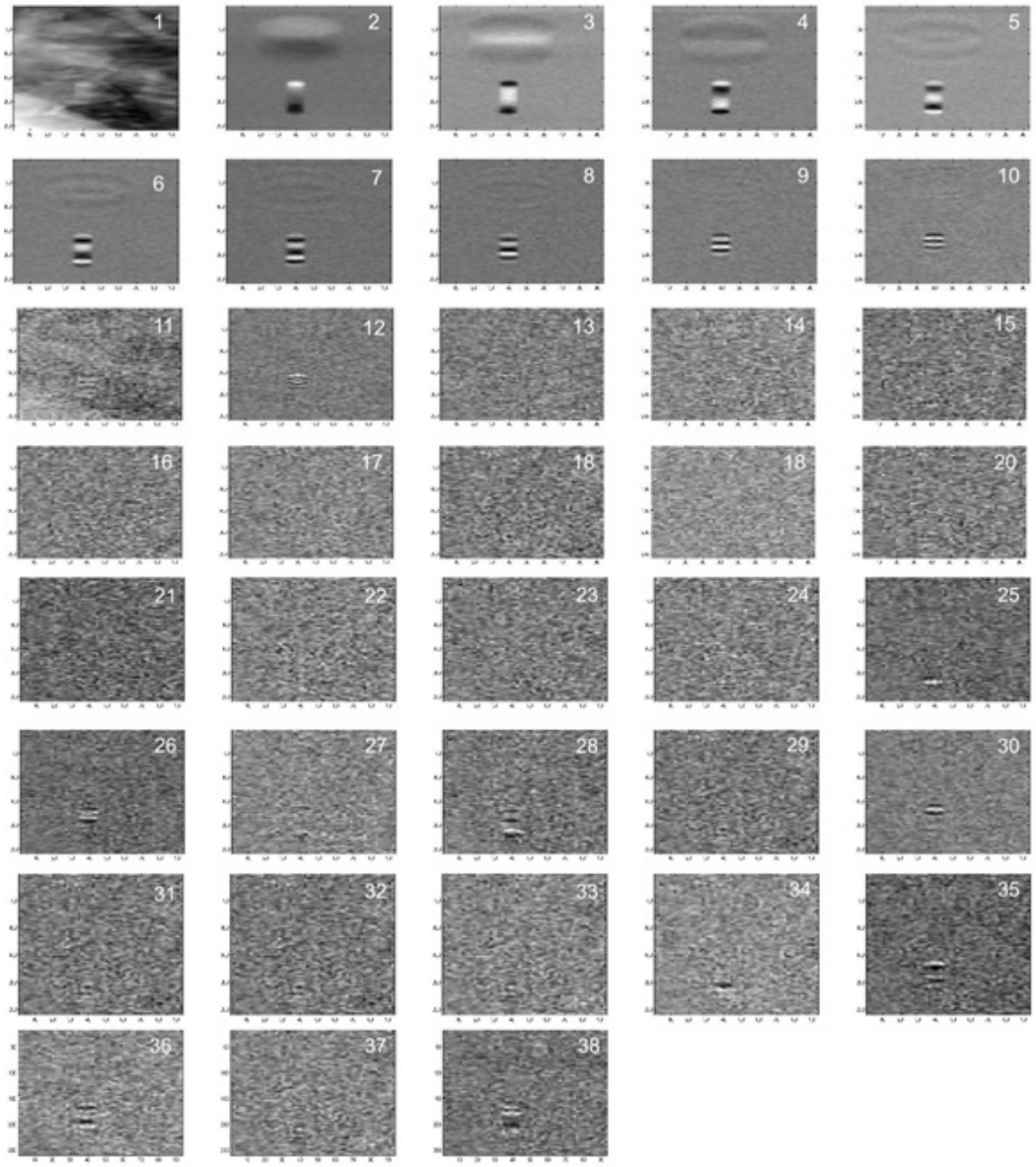

Figure A.2: 38 principal components for kV image.

The score of the eigen value or the principal components is illustrated in Fig.A.3 which shows the logarithmic graph for the different principal component numbers, it can be seen that after 10^{th} component the score goes to almost zero.

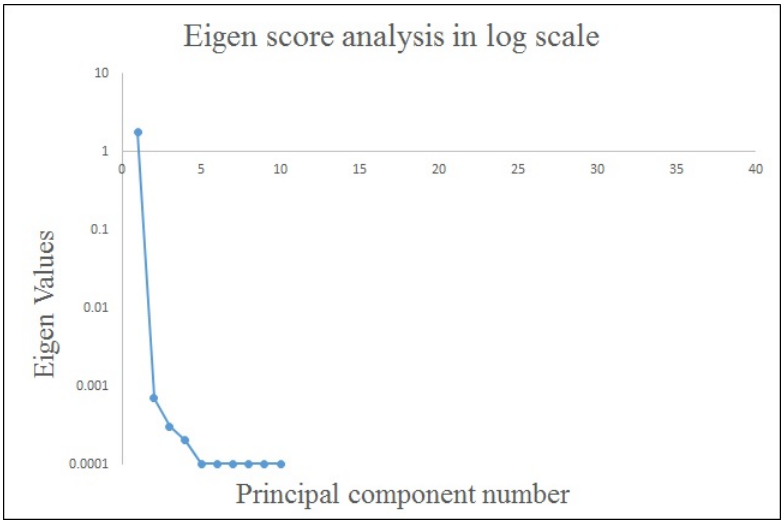

Figure A.3: Eigen score for the different number of principal components for kV images.

Fig.A.4 shows the graph for the different principal component numbers, it can be clearly observed that after 20^{th} component the correlation goes on decreasing. Hence considering the minor component here deteriorates the results instead of increasing the accuracy.

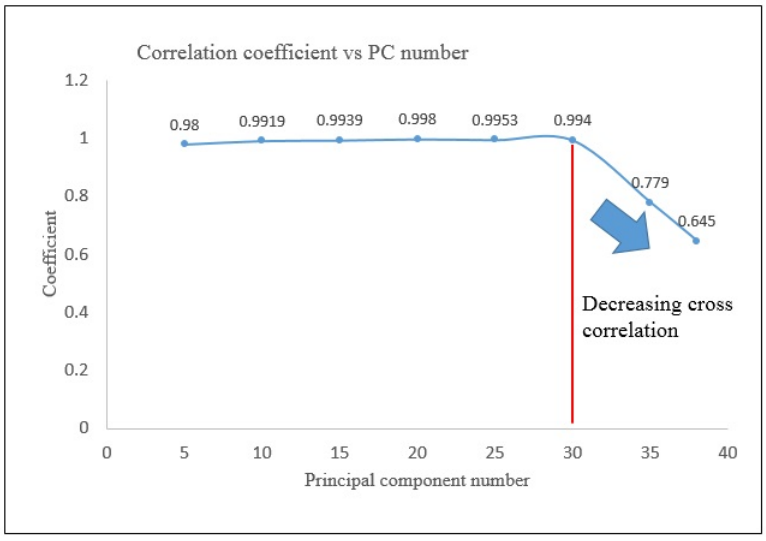

Figure A.4: Analysis for different number of principal components.

A.1.2 Minor components in 4DCT images

Similar analysis was performed for 4DCT images, Fig. A.5 shows the 20 principal component images in which the first image has almost all the feature of the image.

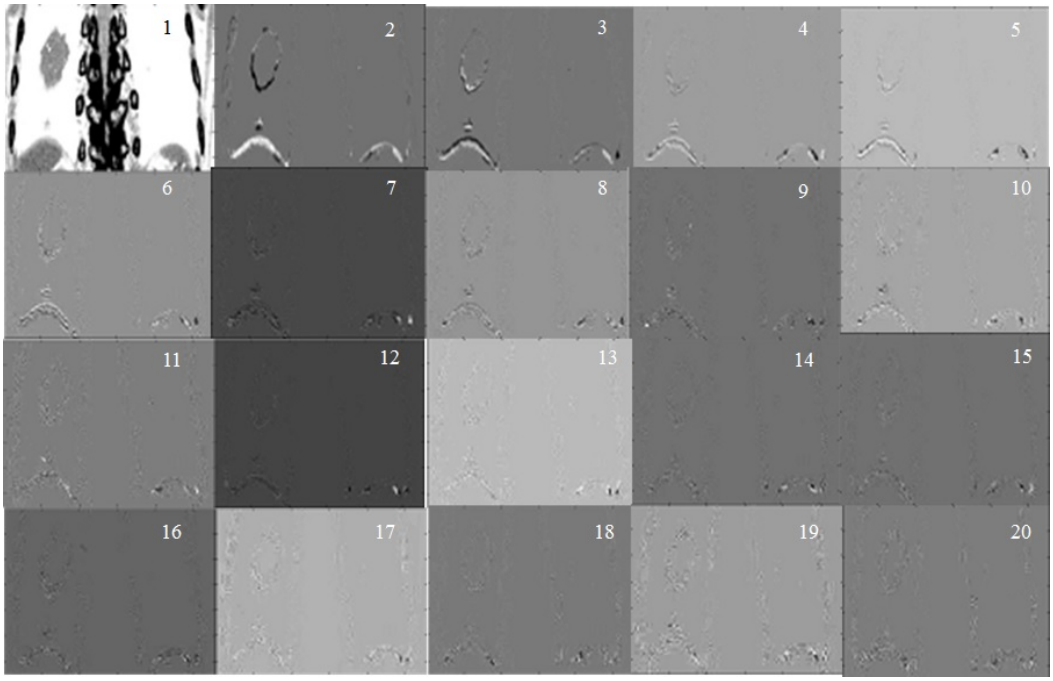

Figure A.5: 20 principal components for 4DCT image.

The score of the eigen values as illustrated in logarithmic plot is shown in Fig. A.6. It shows almost zero value for the other components except for the first three ones.

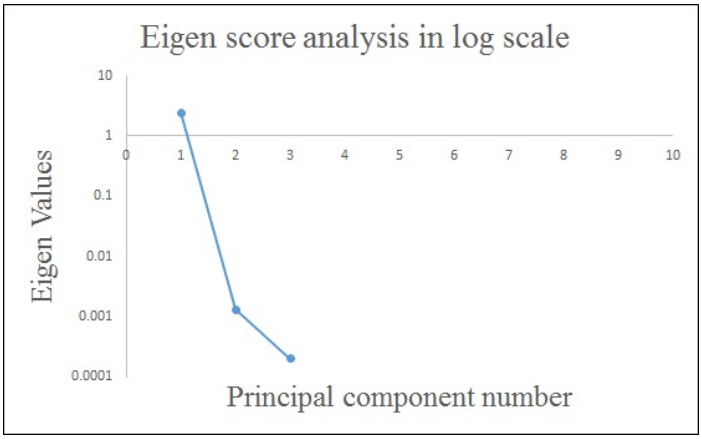

Figure A.6: Eigen score for the different number of principal components for 4DCT images.

Fig. A.7 shows that there is not much change in value of the correlation coefficient does not change much even after increasing the number of principal component.

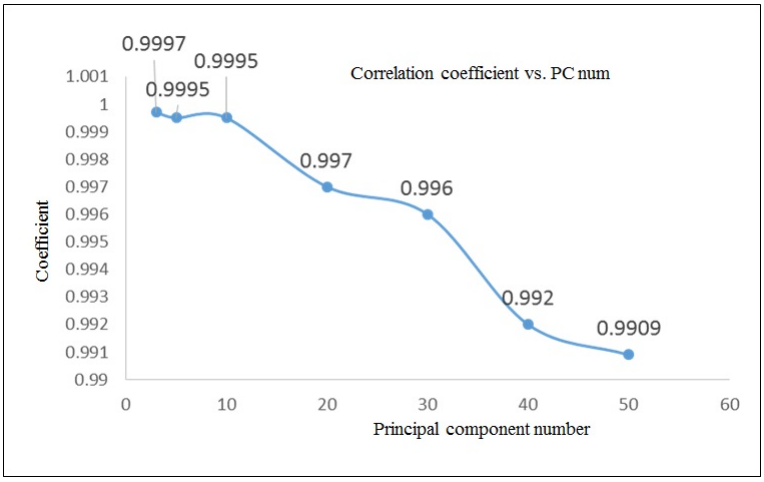

Figure A.7: Analysis for different number of principal components for 4DCT.